The Structure and Stress Development of Adsorption, Impurity Incorporation, and Temperature Controlled Morphology for Thin Films

by

Jordan Kennedy

A Dissertation Presented in Partial Fulfillment
Of the Requirements for the Degree
Doctor of Philosophy

Approved November 2011 by the
Graduate Supervisory Committee:

Cody Friesen, Chair
Peter Crozier
Karl Sieradzki

ARIZONA STATE UNIVERSITY

December 2011

ABSTRACT

There is an inexorable link between structure and stress, both of which require study in order to truly understand the physics of thin films. To further our knowledge of thin films, the relationship between structure and stress development was examined in three separate systems in vacuum. The first was continued copper thin film growth in ultra-high vacuum after adsorption of a sub-monolayer quantity of oxygen. Results showed an increase in compressive stress generation, and theory was proposed to explain the additional compressive stress within the films. The second system explored was the adsorption of carbon monoxide on the platinum {111} surface in vacuum. The experiments displayed a correlation between known structural developments in the adsorbed carbon monoxide adlayer and the surface stress state of the system. The third system consisted of the growth and annealing stresses of ice thin films at cryogenic temperatures in vacuum. It was shown that the growth stresses are clearly linked to known morphology development from literature, with crystalline ice developing compressive and amorphous ice developing tensile stresses respectively, and that amorphous ice films develop additional tensile stresses upon annealing.

ACKNOWLEDGMENTS

No words can express the debt owed to my parents for the efforts they went to in raising me. My Ph. D. is a testament to the love they have shown me and I can only hope to teach the children I will one day have as well as my parents have taught me. They are truly amazing people.

I am sincerely grateful to my advisor to the scientific playground that he provided me with during my studies. Tolerating the general chaos that was associated with my presence was no small feat and is appreciated as it allowed me to grow intellectually. As I move forward in my career I will always value the skills and knowledge gained under his tutelage.

I also owe this accomplishment to my fellow group members. Sharing in the woes and joys of graduate school with them is an irreplaceable experience, and I would like to thank several of them specifically. Erika Engstrom for being a source of common sense, much needed as I occasionally had glaring instances of the lack of such. Lawrence Mickelson, whom I have known for the longest, for being an example of true scientific curiosity. Thomas Heaton for exemplifying tenacity even in the face of massive experimental challenges. Jungwoo Nah for his pursuit of perfection in his studies. Robert Zeller for providing a near inexhaustible source of peculiar information and interesting thoughts.

Finally I want to thank my grandfather David Lambert. If I can even become half the person he was I will consider my life a success.

TABLE OF CONTENTS

CHAPTER Page

CHAPTER Page

CHAPTER Page

LIST OF FIGURES

Figure Page

Figure Page

Figure Page

CHAPTER 1

INTRODUCTION

1.1 Dissertation Structure

This dissertation is structured to give the reader a full understanding of the works conducted by the author during his Ph.D. studies. Chapter 1 will explain the structure of this document and the purpose of each section. The chapter will also orient the reader to the theme of these studies along with the motivation for conducting the experiments and their importance. Chapter 2 defines the fundamental physics and phenomena that are at the core of the research presented in this dissertation. Chapter 3 provides a literature review of previous works that not only give the history of the field, but also provide a means to show the theme of stress-structure relationships as described in Chapter 1 in a well defined manner. Chapter 4 provides general experimental details non-specific to the works in this document and also describes how the various tools and devices used operate. The purpose of this is to give the reader the basic background of the practicalities of working in vacuum so that approaching the experimental details in Chapters 5, 6 and 7 is more straightforward. Chapter 5 describes the change in growth stresses of a copper thin film due to the adsorption of sub-monolayer quantities of oxygen on an existing copper growth surface. Discussion will center on how the presence of oxygen alters the structure of the growing copper and how that impacts the continued growth stresses. Chapter 6 details experiments conducted for the adsorption stresses of carbon monoxide on a platinum {111} surface. The results will show how the stress changes as the structure of the

adsorbed carbon monoxide develops. Chapter 7 consists of works involving the growth of ice films at low temperatures and pressures. Ice grown at these conditions develops two distinct structures (amorphous and crystalline) based on the growth temperature and the experiments performed show that those structures exhibit characteristic growth stresses. Arguments are given as to how these structures create the stresses. In addition, experiments involving the annealing of the ice films after growth will show the stresses associated with thermally induced structure changes. Chapter 8 will propose future works that could further research in this field as related to the work presented in the dissertation. Chapter 9 will conclude the dissertation with closing remarks.

1.2 Motivation and Theme

The theme for the works presented in this dissertation is the relationship between structure and stress evolution at the "nano" scale. The structure of a solid body determines the energy state of the solid's composing atoms relative to other arrangements that these atoms could assume. The differences in these energies results in driving forces for such phenomena as diffusion, phase transitions, plastic deformation, and elastic strain. The driving forces for elastic strain and plastic deformation are then the aforementioned stresses within the solid. It is the path from structure to energy to stress and the link between these that is explored through the research presented in this document. To begin this exploration, it is prudent to define surface stress, give cause to operating at the nano-scale, and provide some practical motive for studying these systems.

Surface stress is the term used to describe the forces present at the surface of a solid. These forces result in negligible bulk stresses when considering systems in which the surface-to-volume ratio is small, but become significant when the ratio becomes large enough. Generally, this is in the "nano" regime, where a characteristic length drops below 100 nm (nanoparticles and nanorods with a diameter < 100 nm, for instance) and is one of the reasons this length scale is of scientific interest. In such systems, the bulk stress induced by the surface stress can reach values as large as several GPa, modifying the stress-state in systems such as micro electro-mechanical systems (MEMS) and microelectronic devices and their electrical interconnects (e.g. electromigration), and leading to a reliability concern (Fu 2004, Wilson 2007, Huang 2010). This has spurred the study and development of the field of surface stress beyond its historical roots as a backwater of the study of the thermodynamics of finite systems (Gibbs introduced the concept of surface stress in his original works, yet literally only a handful of scientists worldwide understand its meaning or implications). Through the exploration and eventual understanding of the physics behind surface stress, practical solutions to surface-stress induced failure can be developed. For this reason, as well as for the satisfaction of human curiosity, surface stress has become a research area of scientific importance.

CHAPTER 2

BACKGROUND

2.1 Thermodynamics of Surface Stress

It is important to begin with a clear definition of the forces that arise at a solid surface. These forces were originally defined thermodynamically as a surface tension in the 1950 paper by Shuttleworth (Shuttleworth 1950), but as the field developed the name of these forces was changed to surface stress so as to discriminate between the liquid and solid cases. The Surface stress has units of force per unit width, and is defined as:

$$f = \gamma + \frac{\delta \gamma}{\delta \varepsilon} \tag{2.1}$$

where f is the surface stress, ε is the strain, and γ is the surface energy. This equation is most easily derived from what is called the Shuttleworth cycle, shown below:

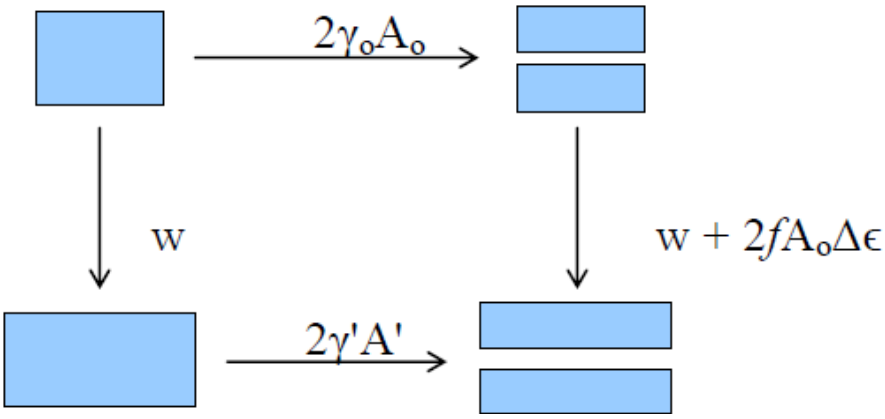

Figure 2.1. Schematic of the Shuttleworth cycle representing two independent reversible paths to create a strained surface and the work performed in each.

The diagram depicts two different routes to create a pair of infinitesimally strained surfaces. Starting at the top left and going clockwise, the path involves the work of creating two surfaces and then straining those surfaces. The other path going counter-clockwise involves straining the sold first, then creating two surfaces out of the strained solid. Since both paths are reversible and have the same starting and ending configurations they are equivalent, and once simplified result in eq 2.1 (Cammarata 1994). Note that γ is also the surface tension observed in a liquid, which is why the solid case uses the surface stress term. To further develop this point, it is useful to compare a liquid, in which f and γ are equivalent (as = 0) to a solid, in which f often differs from γ. The surface of a liquid has an equilibrium number of molecules at a higher energy state than those in the bulk liquid due to the reduced availability of neighboring molecules with which to bond. This energy is collected in the γ term and defined relative to a unit area. When the liquid is strained the system may accommodate the strain either

by increasing its intermolecular spacing, cleaving, or by molecular motion that introduces new molecules to the surface. The most energetically favorable of these strain accommodating methods is the process of molecular motion, as it allows the intermolecular spacing to remain at equilibrium and the only energy cost to the system is the introduction of new molecules from the bulk to the surface. The surface molecular densities of the strained and unstrained cases are identical and thus γ remains constant. As such, the force required to create new area from straining, f, is identical to γ. This differs from the solid case, in which significant molecular motion is prohibited. Of the remaining two options, cleaving and modification of intermolecular spacing (bond stretching), the latter method is the most energetically favorable for small strains. When the strain is accommodated by bond stretching, the surface molecular density is not identical. This means that the force required to strain the surface not only includes creating new surface, but also a term to account for surface modification. This modification is captured in the $\delta\gamma/\delta\varepsilon$ term. For a solid the force required to strain a surface, f, includes both γ and $\delta\gamma/\delta\varepsilon$ as seen in eq 1. There is no surface modification during straining in the liquid case, resulting in $\delta\gamma/\delta\varepsilon = 0$ and $f = \gamma$. For a thin solid body, there are not only stresses that are attributable to the surface but also stresses that are attributable to factors within the bulk.

2.2 Bulk Stresses

Bulk stresses are those that result from processes sufficiently far away from the surface so that the effects of the surface are negligible. These processes generally result from strains induced by the movement of molecules to lower energy configurations within the bulk film. A prototypical example is the annihilation of grain boundaries during grain growth in polycrystalline films. The grain boundaries are regions of disorder and have associated excess void space. When the boundary and void space is annihilated, the material must strain in order to accommodate the void space. When the material is constrained, a tensile strain results and has been observed experimentally (Thornell 1999). Another example of a process that introduces bulk stresses is the inclusion of additional material such as in the uptake of hydrogen by palladium, wherein hydrogen moves within the palladium matrix and occupies interstitial sites. In order to accommodate the additional hydrogen atoms, the palladium expands from its equilibrium spacing. If the material is constrained, this expansion results in the development of a compressive stress within the palladium matrix (Engstrom 2011).

CHAPTER 3

METALLIC THIN FILMS

3.1 Initial Growth

Formative works measuring changes in surface stress focus on the growth of metallic thin films in vacuum. These works create an understanding of the structural and stress developments within the films and the theories linking them. There are several reviews that cover this information, namely those by R. Koch and Doerner and Nix (Koch 1997 and Doerner 1988). While entire books can be written about the intricacies of these systems, a summary of the phenomena is presented below.

The first areas of consideration are the initial growth of a film and its resulting morphology, which have been primarily explored using scanning tunneling microscopy (STM) (Neddermeyer 1990 and Lagally 1993), scanning electron microscopy (SEM) (Venables 1980), and tunneling electron microscopy (TEM) (Pashley 1966). Generally, the initial growth of these systems consists of a clean substrate material with an impinging flux of molecules in vacuum. The behavior of these molecules as they collect on the substrate and nucleate into crystals has been found to develop in three ways. For initial growth, the three archetypes are Volmer-Weber (VW), Frank-Van der Merwe (FM), and Stranski-Krastanov (SK) growth, all shown pictorially below:

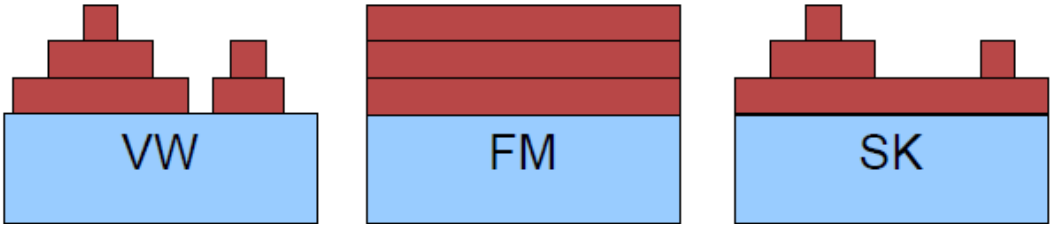

Figure 3.1. Schematic of the three growth modes commonly observed in thin films. The light blue area represents the substrate and the dark red areas represent continuous layers of deposit. From left, the growth modes are Volmer-Weber (VW), which grows in independent islands on the substrate, Frank-Van der Merwe (FM) layer-by-layer growth, and Stranski-Krastanov (SK) growth, in which an initial wetting layer is followed by growth of independent islands.

Each of these modes arises from thermodynamic consideration of the relative free energies of the substrate surface γ_s, the deposit surface energy γ_d, and the interface energy β between the deposit and substrate. To determine the growth mode, these energies are compared as in eq 3.1 below,

$$\gamma' = \gamma_d + \beta - \gamma_s \tag{3.1}$$

where γ' is the energy required to increase the surface coverage of the deposit. If γ' is positive, then it is energetically favorable to reduce the area of the deposit at the expense of exposing the underlying substrate. This results in VW mode growth, which results in the exposure of the substrate surface. If γ' is negative it is energetically favorable to increase the deposit area in order to eliminate the

exposed substrate. This results in wetting and induces FM and SK growth modes. Differentiation between FM and SK growth modes is possible when eq 3.1 is reapplied to incorporate the wetting layer. This results in new γ_s and β values and changes the resultant γ'. If γ' is positive, the system converts to SK type growth. However, if γ' is negative the system continues on in FM type growth.

3.2 Coalescence

As growth continues, new phenomena occur, specifically with the VW and SK growth modes (Koch 1994, Klokholm 1968, Wilcock and Campbell 1969, Wilcock 1969, Abermann 1986, and Abermann 1990). The island type growth matures as shown below in Figure 3.

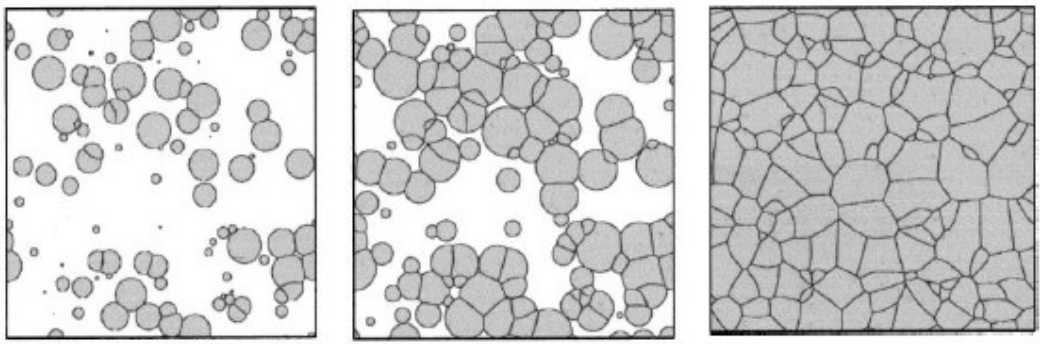

Figure 3.2. Illustration of the growth of a VW (or SK following the wetting layer) in its progressive stages. On the left is shown the nucleation of individual islands. he middle image depicts coalescence and island impingement, and on the right is shown continued bulk film growth. Reproduced with permission from (Seel 2000).

The first stage is nucleation and occurs as discussed above. The second stage is coalescence, in which individual islands begin to impinge on one another as they grow laterally and vertically. Then, depending on the temperature of the system, the film will continue to grow in either Type 1 or Type 2 mode. In both modes individual grains will grow, but the nature of this growth differs.

3.3 Continuous Film Growth

Type 1 growth occurs at low temperatures where atom mobility is restricted. This growth mode is observed at room temperature in materials with high melting points such as tungsten. When the individual islands impinge, the mobility of atoms is too low to allow for significant flux from one grain to another. This limits growth to the inclusion of incoming flux and existing islands will remain within the film. Favorably oriented grains grow faster and occlude the other grains in the film, resulting in a film with a higher ratio of similarly oriented grains. Films exhibiting significant orientation preference are called textured films. The texturing is the direct result of the inhomogeneity of the surface energy of the grains. Grains with low surface energy are more favorable thermodynamically and thus grow more rapidly.

Type 2 growth occurs in materials with lower melting points and is observed at room temperature for such metals as silver, gold, and copper. Type 2 growth is similar to Type 1 growth in that preferential grains with favorable crystallographic orientations grow. However, in Type 2 growth bulk diffusion is also active. This allows for Ostwald ripening to occur which results in growth of preferential grains becoming larger and unpreferred grains being consumed

(Ostwald 1887 and Zinke-Allmang 1992). The driving force for grain consumption is the elimination of grain boundaries, which have an energetic cost associated with their existence. By elimination of these boundaries through grain growth the system as a whole can lower its free energy.

Thus far film nucleation, coalescence, and growth have been discussed with respect to both structure and thermodynamic driving forces. Associated with each of these stages are stresses that develop within the film. These stresses, along with their causes, are discussed later on. As a prelude, it is appropriate to discuss how these stress measurements are made.

3.4 Thin Film Stress Measurement

The most common method for stress measurement is observation of the curvature of a substrate as acted upon by the forces within a film constrained to the surface of a substrate. This was originally pioneered by Stoney in 1909, where nickel was deposited electrolytically on steel cantilevers (Stoney 1909). The force within the nickel film caused the steel to bend and Stoney derived a relationship allowing him to estimate the force in the film based on the curvature of the substrate. The derivation presented below is adapted from the one found in *Thin Film Materials* by L.B. Freund and S. Suresh (Freund 2003). The derivation begins with a system consisting of a disk (the substrate) of radius R that is acted upon by a distributed force, f, parallel to the surface of the substrate (a stressed film, for instance). This system is represented schematically in Figure 3.3.

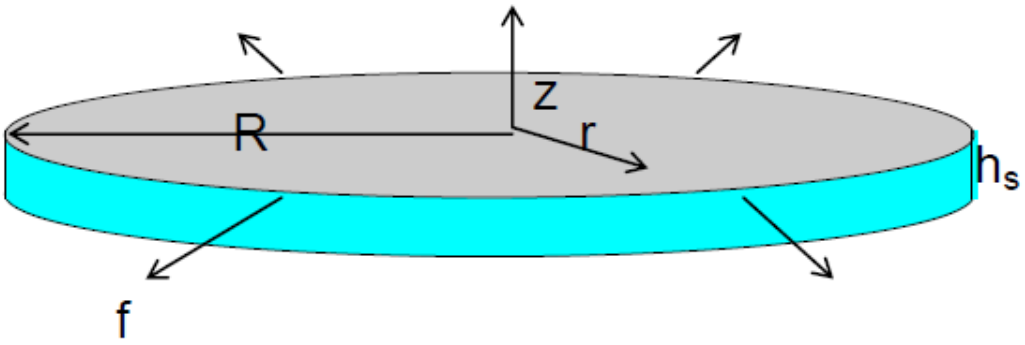

Figure 3.3. Schematic of unrelaxed disk under biaxial force *f* of thickness h_s and radius *R*.

The strain energy density within the system, *U*, is given by

$$U = M_s(\varepsilon_o - \kappa z)^2 \tag{3.2}$$

where M_s is the biaxial modulus, ϵ_o is the extension strain of the disk, and κ is the curvature of the disk. This makes the total strain energy of the substrate, *V*,

$$V = 2\pi \int_0^R \int_{-\frac{h_s}{2}}^{\frac{h_s}{2}} Ur\,\delta r\,\delta z \tag{3.3}$$

where *R* is the total radius and h_s is the disk thickness. The energy in the stress film resulting from the force *f* is given by

$$2\pi R^2 f(\varepsilon_o - \frac{1}{2}\kappa h_s) \tag{3.4}$$

resulting in the total energy of the system given by

$$V = \pi R^2 M_s h_s(\varepsilon_o^2 + \frac{1}{12}\kappa^2 h_s^2) + 2\pi R^2 f(\varepsilon_o - \frac{1}{2}\kappa h_s) \tag{3.5}$$

In order to find the equilibrium state of the system, the energy equation must be minimized. This is performed by differentiating with respect to extensional strain ϵ_o and curvature κ and solving for zero. This results in both

$$\varepsilon_o = -\frac{f}{M_s h_s} \tag{3.6}$$

which is the extension of the disk and

$$\kappa = \frac{6f}{M_s h_s^2} \tag{3.7}$$

which is the Stoney relation defining the curvature of a substrate under a stressed film (Stoney 1909).

In a real system, the forces are quite small and the curvatures induced are also small. It becomes necessary then to develop an apparatus that is capable of detecting small changes in curvature. Generally, these involve clamping a

cantilever on one end and measuring the displacement of the opposite end. This is accomplished either through changes in capacitance or changes in the deflection of a laser beam (Koch 1994). Both methods are depicted schematically in Figure 3.4.

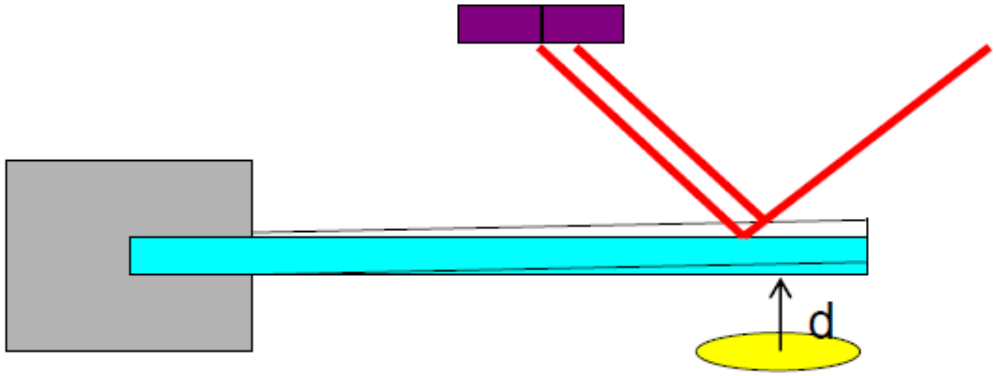

Figure 3.4. Schematic of operating principles for both laser and cantilever based stress monitoring devices. The blue represents a clamped cantilever. The yellow disk represents a sensor that comprises half of a parallel-plate capacitor (the other half being represented by the blue substrate). The laser (red line) is reflected off the substrate and strikes the purple split diode. When the cantilever's curvature changes (as shown by the dashed line) the distance d between the capacitor sensor and the path of the reflected beam (shown by the dashed red line) changes, allowing for detection of the change in curvature.

The deflection of the laser is detected using a split diode, where the relative photo induced current from each diode is compared. This is very similar to common AFM tools that utilize the same principle. As for capacitance based sensors, the

backside of the substrate provides one side of a parallel plate capacitor and an additional sensor comprises the other plate. An applied AC signal is "tuned" to the capacitor formed by the two plates. This tuned frequency is highly sensitive to shifts in the capacitance. This sensitivity corresponds to deflection sensitivity since capacitance, *C*, depends on inter-plate distance as

$$C = \varepsilon_o \frac{A}{d} \tag{3.8}$$

where *A* is the area of the parallel-plate capacitors and ε_o is the permittivity of free space.

3.5 Stresses in Metallic Thin Films

During early investigations of surface stress, experimentalists were unable to produce repeatable results, leading to a transition from high vacuum (HV) to ultra-high vacuum (UHV) conditions and thereby enabling repeatability(Koch 1994). R. Abermann performed a series of experiments that elucidated the cause of the early lack of repeatability by varying the partial pressure of oxygen. The results of Abermann's experiments are reproduced in Figure 3.5.

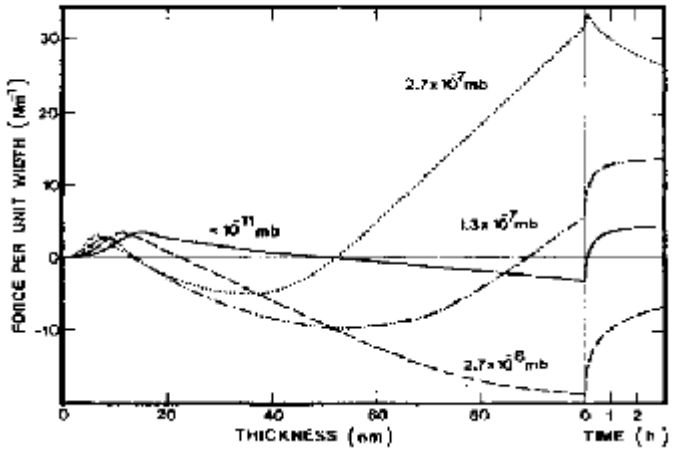

Figure 3.5. Plot of stress versus thickness of copper grown on MgF_2 as a function of oxygen partial pressure. Reproduced with permission from (Abermann 1986).

Note the sign change in the slope of the stress induced by relatively low partial pressures of oxygen on a developing copper film. It is for this reason that quality UHV equipment is needed in order to produce the experimental environment necessary to conduct these experiments.

The results obtained from these studies found two prototypical types of stress versus thickness plots for growing films. The two types of plots are associated with the Type 1 and Type 2 film growth cases as discussed earlier. These plots are reproduced below in Figure 3.6.

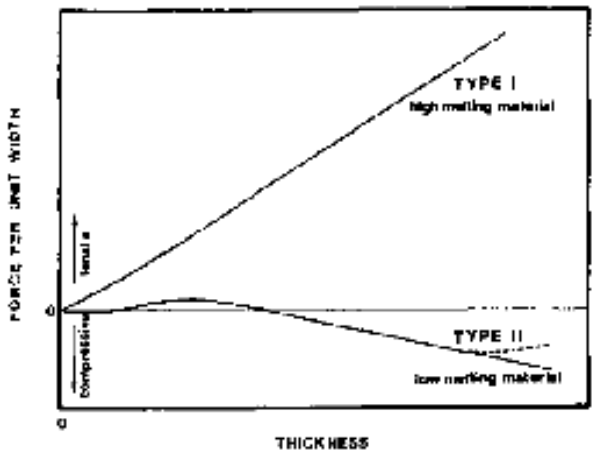

Figure 3.6. Representative plot of the growth stresses for Type I and Type II thin films. Reproduced with permission from (Abermann 1990).

Type 1 film growth has a long term tensile growth stress that is linear once stable growth has been achieved. Due to the kinetic limitation imposed on the system by low temperature, there generally is an excess of void-type defects within the film, causing the tensile stresses that are observed as the material attempts to condense and eliminate void space.

For Type 2 film growth stresses, the curve identifies three regions: a compressive regime associated with island nucleation, a subsequent tensile regime associated with coalescence, and a final long-term compressive stress that is attributed to continued growth. The initial compressive regime is thought to originate from compression of the lattice spacing of an island nuclei due to the tensile stress state of the surface (Mays 1968). This compression is analogous to the Laplace pressure difference between the inner and outer gas volumes of a bubble.

As the island size increases the compression from surface effects drops, but due to traction with the substrate the shortened lattice spacing is maintained and the island nuclei enter the observed state of compression (Abermann 1986, Laugier 1981, Floro 2001, and Cammarata 2000). Further growth continues to maintain the shortened lattice spacing, further generating compressive stress until the tensile stress from coalescence begins to dominate.

The tensile stresses observed following nucleation correspond to a phenomenon known as island "zipping", which occurs when two neighboring islands strain together to eliminate surface area in exchange for grain boundary area. Models for this originate from Hoffman and Doljack with significant improvements offered by Nix and Clemens (Hoffman 1966, Hoffman 1976, Doljack 1972, and Nix 1999). In the Nix and Clemens model, the islands are assumed to be hemispherical shapes on the substrate surface. At the point of zipping, the island "hemispheres" just touch at their outer points. The purpose of choosing this type of geometry is that it closely resembles the actual morphology of the films and also mirrors the geometry used in some crack closing models, in which there is a competition between elimination of surface area and strain energy. Surface reduction drives the crack closure, and strain energy mitigates the closing of the crack. For the thin film case the islands strain together to trade free surface for grain boundary area. The strain results in the tensile stresses that arise in the film. Other models have built on this simpler model, such as those by S.C. Seel et al., but the basic principles remain the same (Seel 2000).

Eventually, the islands completely coalesce and a continuous film is formed. For this stage of growth the film develops a long-term compressive stress, which interestingly, has not been observed in single crystal systems (Ramaswamy 2001) In single crystal systems, the stress profile rather resembles that of Type 1 growth. Both single crystal and Type 1 systems have little appreciable interaction between incoming flux and grain boundaries as grain boundaries are either nonexistent or kinetic limitations for diffusion to the boundaries are present. In order to explain the long-term compressive stress in Type 2 polycrystalline films and the lack of long-term compressive stress in single crystal and Type 1 films a model based upon the interaction between incoming flux and grain boundaries was proposed (Chason 2002). The model suggests that the incoming flux drives an excess number of molecules into the grain boundaries which then give rise to the compressive stress that is observed in the stress versus thickness plot. When the incoming flux is halted, it is expected that some of these excess molecules will migrate out of the grain boundaries and incite a relaxation in the compressive stress. In Figure 3.5, where the axis changes from thickness to time, such a relaxation is observed. This relaxation is also called reversible stress, because upon resumption of growth the stress returns to its pre-interrupted value. There is still some contention with the grain boundary model, however. Returning to Figure 3.5, a change in the sign of the reversible stress is observed at high oxygen partial pressure, a phenomenon not readily explained by the grain boundary model. Also, C. Friesen and C.V. Thompson gave evidence of reversible stress for a film during precoalescence, a regime in which grain

boundaries are not present (Friesen 2002). To explain reversible stress without invoking grain boundaries, a model focusing on stress generated by surface defects was proposed. In this model, the incoming flux generates an excess of surface defects and upon halt of the flux, the surface tends to an equilibrium structure and eliminates these defects. This argument has also been made by Koch, Dongzhi, and Das (Koch 2005). However, some molecular dynamics simulations indicate that stresses associated with surface defects are insufficient to account for the observed forces (Pao 2006). There is still contention regarding an accurate universal model, making this an active area of research. It is possible that a combination of these models is responsible for the observed stresses, but additional research is required to elucidate this.

CHAPTER 4

GENERAL EXPERIMENTAL DETAILS

4.1 General Structure of a Vacuum Chamber

In this section general experimental details non-specific to the experiments conducted in Chapters 5, 6, and 7 are presented. This includes such information as the aspects of operating in an ultra-high vacuum (UHV) environment, basic operating principles of equipment used, and calibration of cantilevered capacitance based sensors.

UHV is generally accepted to be in the range of 1×10^{-8} Torr or below. At 1×10^{-8} Torr the nominal time it takes a layer of adsorbates to form is of order 20 minutes and gives an upper bound for pressures at which gaseous species may be neglected during experimentation. To reach such pressures, a combination of pumping power, cleanliness, and appropriate sealing must be applied against the atmosphere.

Generally, an effective pumping system consists of a mechanic roughing pump to reach 1×10^{-3} Torr, a turbo-molecular pump to reach 1×10^{-7} Torr, and a gettering pump such as a cryo-pump or ion-pump to reach the ultimate base pressure below 1×10^{-8} Torr. Mechanical roughing pumps operate by the simple mechanism of opening a volume to the vacuum, in-taking gasses from the vacuum, then ejecting said volume to atmosphere. Usually located in front of the roughing pump is a turbo-molecular which operates by kinetically driving the gasses from the intake to the outlet. Resembling a jet turbine, arrays of blades rotate at up to 15,000 rotations per minute closely to opposing arrays of stators.

The blades impart kinetic energy to the gas molecules and drive them to the outlet. Due to the high rotation rates of turbo-molecular pumps and the requirement for the pumped gas to nominally obey the kinetic law of gasses, the pressure of the chamber must drop below a pressure threshold of around 1 x 10^{-2} Torr otherwise the pump will not operate effectively and will often overheat. Cryo-pumps, which bring the vacuum chamber to its ultimate operating pressure, do so by thermally trapping gas at what is termed the "cold head". Cryo-pumps cool the cold head by cyclically compressing and expanding helium gas at the compressor and the cold head respectively, acting as a heat pump. Reaching temperatures of 17 K and below, these devices freeze and collect gasses as opposed to expelling them from the chamber. Due to this, cryo-pumps must be periodically heated to desorb the accrued gasses as part of their maintenance. The gettering operating principle also requires pressures below 1 x 10^{-5} Torr, otherwise the pump will rapidly saturate and the pumping efficiency will decline. The combination of all these pumping mechanisms compete against the continuous introduction of gasses from various sources to determine the ultimate pressure of the chamber.

4.2 Leaks

One of the most critical type of sources for the introduction of gasses into a vacuum chamber is contaminants with significant vapor pressures. Skin oil, for instance, remains on a contaminated piece of equipment for extended periods of time and continuously evaporates into the chamber raising the pressure within the chamber and also contaminating any sample surfaces. For this reason extra care

is needed to avoid contamination of any surface that is exposed to the vacuum. Vinyl gloves must always be worn when handling UHV equipment and special tools used. These tools need to be carefully cleaned and made from materials such as steel that will not contaminate equipment. The handles on screwdrivers, as an example, cannot be a soft rubber and instead should only be a hard plastic. Other unexpected sources of contamination originate from high vapor pressure metals such as those found in solder. For this reason making electrical connections in vacuum is not a trivial endeavor. Contaminants are only a part of what introduce gasses into a vacuum chamber, however.

True leaks dominantly come from failed seals prevalent in a vacuum chamber. Viton seals, a vacuum compatible polymer, are commonly used at openings that must be consistently opened and closed during operation of a chamber. If a small piece of solid matter is located on the surface of the Viton, it will deform the Viton and create a gap to allow entry of gasses. For this reason these seals should be consistently checked for foreign objects. Long term seals are generally made through the use of two steel knife edges that imbed themselves in a copper ring. The copper deforms to accommodate the steel knife edges and creates a seal. Failure of these seals, although rare, can occur when the seal is created asymmetrically. The asymmetric creation of the seal can result in gaps which would allow the passing of gas into the chamber. Another common seal is associated with the closed piping of cooling water into and out of the chamber. Connections for the piping within the chamber generally consist of two polished convex surfaces pressing into and deforming a metal plate, similar to the

previously mentioned copper seals. These seals also have a similar failure mechanism, although it is quite rare. One of the most delicate type of seals are those found between an insulator and a metal, such as those found in view-ports and for electrical feed-throughs. Failure of these seals can either come from physical impact or thermal expansion mismatch from heating. In both cases the insulator usually cracks and begins to allow gas through the seal.

4.3 Vacuum Equipment Related to Thin Film Growth

There is a host of equipment that is used in conjunction with the vacuum chamber in order to conduct experiments in vacuum. These include sputter guns, electron beam evaporators, quartz crystal micro-balances, heating stages, thermocouples, thermocouple gauges, ion gauges, and leak valves. Each are discussed in regards to their use and operating principles.

Sputter guns are a primary method for the deposition of thin films from a variety of materials. Sputter guns operate by applying a high bias (of order 100 V) to an inert gas such as argon to ignite a plasma and then drive this plasma into the material that is to be deposited. A strong magnetic field is used to corral the charged ions into a tight ring at the surface of the target. Through the physical impact of the ions, the target material is kinetically ejected outward and then adheres to the substrate placed opposite of the target. Due to the presence of the inert gas at a pressure of around 1×10^{-3} Torr, the path of the deposited material is not perfectly line-of-sight.

For this reason mask lines will not be sharp if the mask is not adjacent to the substrate. Since a strong magnetic field is required to direct the ions, magnetic materials are generally avoided for deposition with a sputter gun.

Electron beam evaporators are an additional method for the deposition of materials and the creation of thin films. Initially, a filament is resistively heated to thermally excite electrons. These electrons are then accelerated through the application of a several kilo-volt potential from the filament to the material to be deposited. The path of the electron beam is controlled through the use of magnetic fields. Electromagnets can be utilized to dynamically alter the path of the electron beam, which allows for even heating and stirring if the material becomes molten. The electron beam heats the material until the material begins ejecting mass in the form of a vapor. This vapor then deposits on the substrate. Electron beam evaporators operate at significantly lower pressures than sputter guns and as such the deposition is line-of-sight. Masks located some distance from the substrate can still result in sharp deposition lines. The material to be deposited is generally held in a crucible liner. Crucible liners are often carbon, but should be selected to be compatible with the material to be deposited. Some materials, such as aluminum and platinum, are prone to splattering and are poor choices for electron beam evaporators.

In order to control the rate at which a film is deposited, and the ultimate thickness of the film, a device called a quartz crystal micro-balance (QCM) is employed. A QCM is a quartz crystal where an oscillating potential is applied across the crystal. Since quartz is a piezoelectric material, the crystal will deform

in response to the applied field. As mass is deposited on the crystal, the crystal's resonant frequency changes. By tracking the resonant frequency of the crystal with electronics, the mass deposited can be calculated along with a deposition rate. Due to the myriad of factors impacting the resonant frequency shift versus mass, along with geometry of the deposition, it is necessary to implement a tooling factor and periodically calibrate the QCM. It is also important to maintain a constant temperature for the quartz crystal through the use of cooling water circulation, as temperature variations significantly affect the accuracy of the QCM. The electronics associated with a QCM generally also contain a feedback loop to an output that can alter the power of a deposition source. Through this, a consistent rate of deposition is maintainable even without operator interaction.

As discussed in Chapter 3, the temperature at which a film is deposited can dramatically affect both the stresses and structure that a film develops as it grows. In order to experimentally alter the temperature, it becomes necessary to heat a sample in a controlled manner through the use of a heating stage. One of the most straightforward methods is to have a filament array behind the sample that is resistively heated. The filament then heats the backside of the sample through radiative emission. There is a bit of finesse in properly heating a sample. Unless the thermometer used to measure the sample temperature is directly affixed to the substrate, there can be significant differences in measured temperatures and actual sample temperatures.

Also, there is a temporal component to heating, as the heat has to oftentimes diffuse through material to the substrate and to the thermometer. A consequence of this is that not only sample temperatures must be given sufficient time to equilibrate, but growth recipes for one deposition chamber may not transfer to other chambers.

Thermocouples, a type of thermometer, are a rapid and accurate way to measure temperature electronically. These devices operate by the contact between two dissimilar metals. Due to the relative Fermi levels and electronic properties of the two metals, a bias voltage develops between the two materials as they are heated. This bias can be measured and the temperature of the junction measured. Since the reading is a voltage, electronics can interpret this signal and use it in conjunction with a feedback loop to control the temperature of a sample. This is similar to the previously mentioned QCM electronics.

4.4 Vacuum Equipment Related to Pressure Measurement

There are multiple ways to measure the pressure within a vacuum chamber. A thermocouple guage is a prominent tool for pressure ranges between atmospheric and 1×10^{-3} Torr. The device works by having a small heat source opposite a thermocouple. The heat is then conducted to the thermocouple by the gas present within the chamber. Naturally, the greater quantity of gas in the chamber results in more heat transferred to the thermocouple. By measuring the temperature of the thermocouple, the pressure within the chamber can be inferred. However, the device becomes inaccurate and ultimately useless as the pressures drop below 1×10^{-3} Torr.

For measuring pressures below 1 x 10^{-4} Torr, an ion gauge may be used. The device operates by ionizing the gasses near a collector by electron excitation. As the charged ions discharge into the collector, a current is developed. At a higher the pressure more gas molecules get ionized and result in a higher current. Thus the current is a measure of the pressure within the chamber. Since the ion gauge uses a filament for electron emission and creates ionized gas, the gauge cannot operate above 1 x 10^{-4} Torr without risk of damage to the filament and other components.

4.5 Vacuum Equipment Related to Introduction of Gasses

Sapphire seat leak valves allow for the controlled inlet of gas and steady maintenance of a partial pressure down to 1 x 10^{-9} Torr or better. The operating principle for the leak valve is straightforward, as the sapphire seat simply blocks an orifice leading to the chamber. There is a lever actuated by a finely threaded shaft that moves the sapphire seat relative to the orifice. The flux into the chamber increases as the orifice is opened. The operator can then balance the influx of gas against the pumping acting on the chamber to equilibrate at the desired partial pressure of gas. In order to increase consistency of the leak valve, it is useful to apply a light constant force, such as from a rubber band, against the lever so it does not drift. Also, due to the fine threading on the control shaft, care must be taken to not over-tighten the valve when closing, which risks breaking the sapphire seat.

4.6 The Surface Stress Monitor

The device used to measure surface stress and the protocol used to calibrate the device deserve special attention as they are both critical to the experiments found within this dissertation but are also not “off the shelf” devices.

The basic principles for the operation of a capacitance based stress monitor were discussed in Chapter 3. Several experimental peculiarities arise from these principles that need to be watched for when using such a device. For one, the sensor is quite sensitive to electric fields and charging. Electron beam evaporators require their filaments shielding in order to prevent interference with the sensor. In the case of sputter gun deposition the sensor must be shielded from the plasma cloud or risk charging and discharging noise. When creating a custom sensor (such as that in the experiments for Chapter 8), the geometry consists of the actual sense pad, a shielding shroud held at a specific shielding potential, and the cantilever held at a potential that interacts appropriately with the sense pad. Each of these components must be well insulated electronically against one other, which can be challenging as the sense pad and its leads must be in close proximity and almost entirely enclosed in the shielding. If there is electrical contact between any of the three components the device will not operate properly. In regard to the electronics used, all experiments in this dissertation relied on an ADE model 4810 HS circuit. This outputs a + or - 10 volt signal which was collected and digitized via a National Instruments BNC 2090 data acquisition board. Conversion of the voltage signal into stress requires a calibration step that is explained below.

The calibration utilizes the geometry of the cantilever sample along with material constants to compare an anticipated deflection to the output voltage change during gravity induced deflection of the cantilever (the cantilever is inverted normal to gravity causing a deflection). This yields a deflection per volt number, which is relatable back to a curvature through the cantilever geometry. Finally, this curvature is related to the stress state of a film on the cantilever through the Stoney relation. This is the flow of the calibration process which is repeated mathematically below.

As stated above, the first step is to calculate the anticipated deflection due to inversion against gravity. This is a simple deformable solids problem where a distributed load results in a bending moment on a clamped beam, the results of which are below in eq 4.1

$$d = \frac{\rho g W h_s x^2}{12 E I}\left(x^2 + 6L^2 - 4Lx\right) \tag{4.1}$$

where d is the deflection of the cantilever at a distance x along the beam, ρ is the density of the substrate, g is the acceleration due to gravity, L is the total length of the cantilever, E is the elastic modulus of the cantilever, W is the width of the cantilever, and I the second moment of inertia of the cantilever. We take the calculated deflection d, insert I appropriate for a rectangular beam and divide it by the experimental voltage from inverting the sensor, giving

$$C_g = \frac{\rho g x^2}{E h_s^2} \frac{x^2 + 6L^2 - 4Lx}{\Delta V_g} \tag{4.2}$$

where ΔV_g is the change in voltage from the inversion and C_g is the gravity calibration factor which the input voltage can be converted into deflection with. We then need to convert this deflection into a curvature of the sensor. This is done by considering the cantilever geometry below.

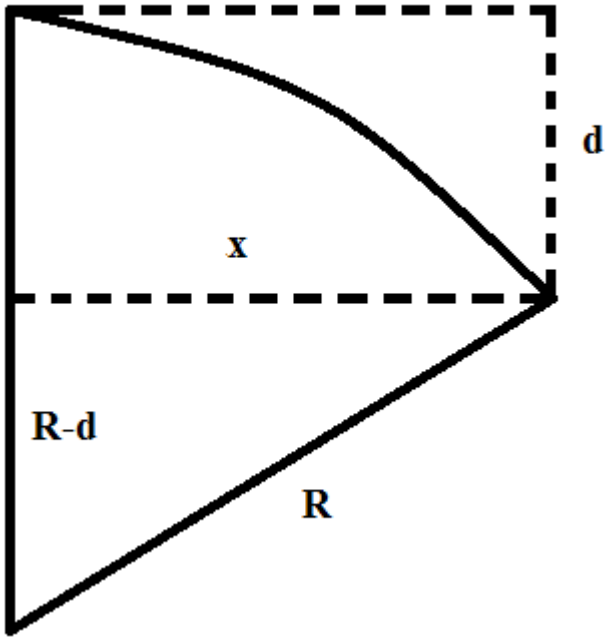

Figure 4.1. Shows the geometry of a bending cantilever. *R* is the radius of curvature, *x* the point at which the deflection is measured, and *d* the deflection of the cantilever at *x*.

The figure shows a highly exaggerated bending and the relative geometries, where *d* is the deflection of the cantilever, *x* is the distance at which *d* is measured, and *R* the radius of curvature which is also the inverse of curvature, κ. Using Pythagoras's theorem *d* and *R* are related as such:

$$x^2 + R^2 - 2\mathrm{Rd} + d^2 = R^2 \tag{4.3}$$

Note that since *d* is very small (of order nanometers) higher order terms consisting of *d* may be ignored with little error, giving

$$R = \frac{x^2}{2\mathrm{d}} \tag{4.4}$$

From here, the Stoney relation

$$\kappa = \frac{6f}{M_s h_s^{\,2}} \tag{4.5}$$

is used to convert the deflection to a film force, resulting in

$$f = \frac{M_s h_s^{\,2} d}{3x^2} \tag{4.6}$$

The final step is to take the input signal voltage from an experiment V_{exp}, multiply it by C_g, and insert that experimental deflection into eq 16 giving

$$f = \frac{M_s \rho g}{3E} \frac{\left(x^2 + 6L^2 - 4\mathrm{Lx}\right)}{\Delta V_g} V_{\exp} \tag{4.7}$$

By recalling

$$M_s = \frac{E}{1-\nu} \tag{4.8}$$

gives

$$f = \frac{\rho g}{3(1-\nu)} \frac{\left(x^2 + 6L^2 - 4\mathrm{Lx}\right)}{\Delta V_g} V_{\exp} \tag{4.9}$$

which is the calibration factor that the raw voltage signal of an experiment is multiplied by to convert it into a meaningful film force. Note that neither the substrate thickness nor the substrate elastic modulus appears in the end calibration, which is beneficial as these can be significant sources of error.

This concludes the general experimental details that are relevant to all the experiments presented in this dissertation. In the later chapters, additional experimental details are presented that are specific to each type of experiment. It is hoped that the general discussion thus far will provide an excellent starting point for understanding why those experiments were conducted in the manner that they were.

CHAPTER 5

COPPER GROWTH AND OXYGEN

5.1 Introduction

This work focuses on copper {111}, a film that grows as a Type 2 VW film at room temperature, and builds on earlier work by Abermann that explored the effects of oxygen partial pressure on the growth stresses of copper {111} as seen in Figure 3.5. Abermann's experiments, however, did not deconvolve gas-phase oxidation, oxygen adsorption, oxygen uptake in the film, oxidation of the surface, nor the amount of oxygen present at the surface. The author's work removed many of these effects, specifically those associated with a partial pressure of oxygen existing during growth, leaving only a well known quantity of oxygen on the surface. The findings showed that even sub-monolayer quantities of oxygen on the surface result in significant and quantifiable changes in the growth stresses of the film.

5.2 Experimental Details

Results from this work were obtained using an ultra-high vacuum chamber with a base pressure of 5×10^{-10} Torr. The copper was deposited using a Thermionics electron beam evaporator. Both the amount of copper deposited and the amount of oxygen adsorbed on the surface of the copper film were measured using a quartz crystal microbalance (QCM). Oxygen introduction was controlled using a sapphire leak valve, allowing precise manipulation of the amount of oxygen adsorbed on the surface. The oxygen partial pressures during adsorption were tracked using a quadrupole mass spectrometer, also referred to as a residual

gas analyzer (RGA). Stress measurements were obtained using a capacitance based cantilever stress monitor as described previously. Calibration was achieved by correlating the gravity induced deflection of the cantilever upon inversion of the device and the output signal received from the device during deflection, described in detail in Chapter 5. The experimental process is shown schematically in Figure 5.1 below.

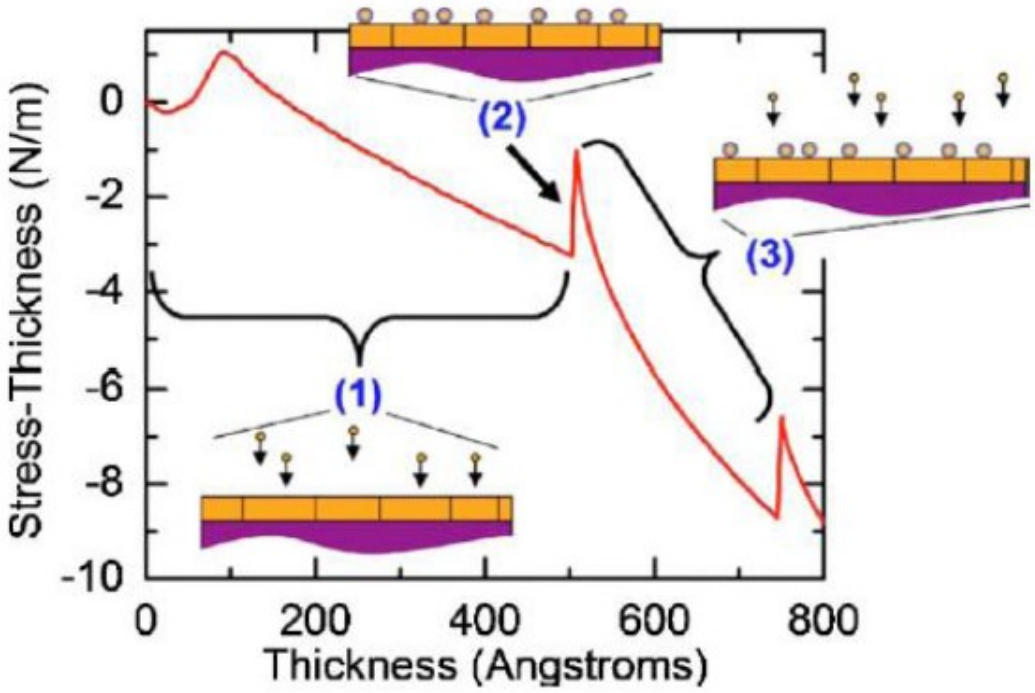

Figure 5.1. Plot of stress-thickness versus thickness for a typical experiment. Region 1 represents copper growth at 1 Å/s. Region 2 is indicative of a 30 minute growth interruption and oxygen dosing, and Region 3 shows continued growth after the oxygen partial pressure falls below 2.5 x 10^{-9} Torr. Reproduced with permission from (Kennedy 2007).

Region 1 in the figure shows the initial growth of the copper film at 1 Å/s, exhibiting characteristics of Type II VW film growth. Region 2 represents the only instance at which a partial pressure of oxygen is introduced into the chamber and occurs when a defined amount of oxygen becomes adsorbed onto the surface. Region 3 indicates resumption of copper growth on the oxygenated copper surface at 1 Å/s after the partial pressure of oxygen drops below 2.5×10^{-9} Torr.

5.3 Results

The results of this work are shown in a collection of plots taken from Region 3 of Figure 5.1, with varying oxygen coverages. As seen in Figure 5.2 below, a marked increase in compressive stress is generated within the growing film upon the introduction of oxygen.

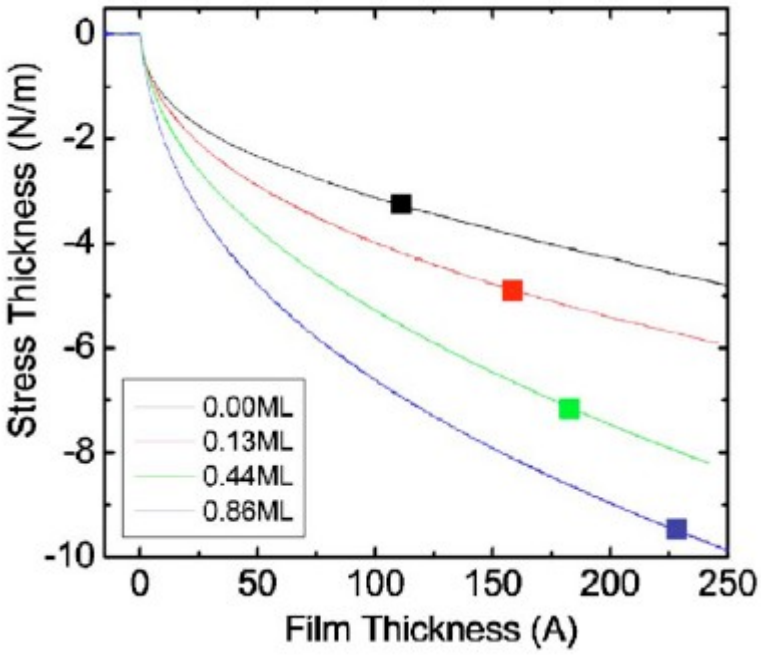

Figure 5.2. Collection of stress-thickness versus thickness plots for continued growth of copper on an oxygen-dosed copper surface. Dosage amounts are represented in mono-layers (ML). Demarcated points are stead-state conditions as defined by eq 20. Reproduced with permission from (Kennedy 2007).

Note that even for a sub-monolayer quantity of oxygen the continued growth stresses can exceed twice the stress magnitudes observed for an oxygen free surface. Of further interest are the points demarcated in Figure 5.2, occurring when the films enter their "steady state" or constant slope regime, defined as

$$\frac{\delta^2(\sigma h)}{\delta h^2} \leq 1\text{x}10^{-20}\frac{J}{m^4} \tag{5.1}$$

5.4 Interpretation of Instantaneous Stress

The significance of these points comes from the physical interpretation of the slope of the plots, which is mathematically defined as $\delta f / \delta\theta$ and accorded the title "instantaneous stress", or the amount of stress that is added for a unit increase in thickness. Physically, if a layer of atoms is added to a surface, a stress change associated with the layer is observed. If the new surface is identical to the old surface and another layer is added exactly as before, the same stress change should occur. This means that the instantaneous stress is a characterization of the surface and its interaction with incoming atoms. Because the growth rate is held constant, it is reasonable to assume that incoming atoms are identical in quantity and properties to their precedents for a given period of time. The only transient that remains is the surface itself and so we conclude that the slope is a direct descriptor of the state of the surface alone. In the case of the oxygen-free surface, the coverage at which a constant slope is achieved describes the time it takes for the surface defects due to the incoming 1 Å/s flux to reach a steady state. For the oxygenated surface, the increase in thickness that accompanies the steady state shows that the oxygen has an influence on the propagating surface and incites a continuous surface change for far longer than it takes to reach steady surface defect states. Figure 5.3 collects these points and plots them for comparison.

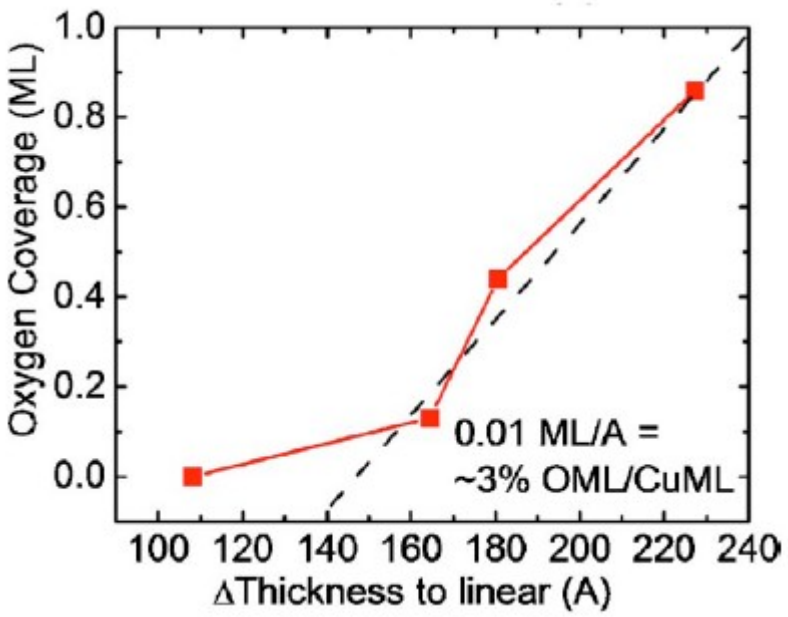

Figure 5.3. Plot of oxygen coverage versus thickness to linearity (defined by eq 20). The fitted line shows what is believed to be the oxygen island occlusion rate. Reproduced with permission from (Kennedy 2007).

It is known that at room temperature oxygen rapidly forms semi-disordered Cu_2O islands when adsorbed on Cu (111) (Matsumoto 2001, Tsay 2001). The islands form preferentially at step ledges where the oxygen diffuses in the (111) plane. New copper grown on these Cu_2O islands would tend to be disordered due to registry effects between the new copper and the Cu_2O island structure. This process should continue until all the registry effects with the underlying Cu_2O have been eliminated and the system reaches steady state, signaled by the instantaneous stress attaining linearity.

This leads to the interpretation that the slope plotted in is the thickness of continued copper growth required to “snow-in” the structural effects induced by the Cu_2O islands. The linear fit to the slope in Figure 5.3 is then an occlusion rate, where 3% of an oxygen mono-layer's structural influence is occluded for each copper mono-layer grown.

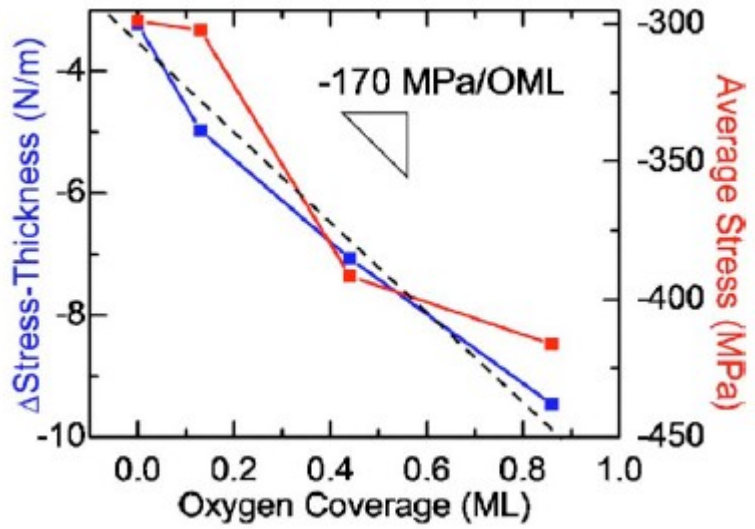

Figure 5.4. Plots of Δstress-thickness and average stress as a function of oxygen coverage (1 ML corresponding to a one to one ratio of adsorbed oxygen atoms to copper surface atoms). The dashed line is a linear fit to the average stress data. Reproduced with permission from (Kennedy 2007).

The values represented in Figure 5.4 are taken from the previously defined steady state. The dashed line is a linear fit to the average stress versus oxygen coverage data, and describes the stress field at complete incorporation associated with the oxygen. The slope of the linear fit indicates that an additional -170 MPa of stress

per oxygen monolayer is incorporated into the film. These stress fields naturally induce a strain in the film and a modification of the lattice parameter of the copper. Figure 5.5 provides some insight into these effects through inspection of the instantaneous stress at steady state.

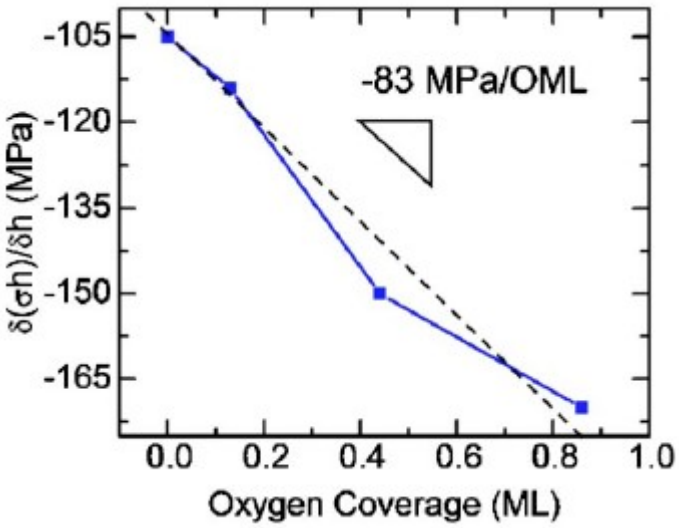

Figure 5.5. Plot of instantaneous stress at complete oxygen incorporation as a function of oxygen coverage. The dashed line is a linear fit to this data. Reproduced with permission from (Kennedy 2007).

It should first be noted that these values are taken at steady state, implying that the structure of the surface is stable. However, the instantaneous stress between each oxygen dose at steady state is different. This indicates that, although all of the oxygen resides in the bulk of the film, the surfaces of these films are fundamentally different in some way. The difference is ascribed to a shift in the surface lattice parameter due to the stresses and strains induced by the

underlying oxygen propagating to the surface of the film. When a new layer of copper atoms is deposited onto the surface, the layer must strain itself in order to maintain epitaxy. It is this strain that causes the increase in instantaneous stress.

This argument parallels Mays' explanation of the compressive stress of VW films from the lock-in and propagation of a non-equilibrium lattice spacing (Koch 1986, Mays 1968, Laugier 1981, Floro 2001 and Cammarata 2000). In Mays' case, the new lattice spacing is due to surface stress and a resulting Laplace pressure. For the case of oxygen in copper, the new spacing arises from the excess oxygen within the underlying film. The dashed line in Figure 5.5 captures the stress state of each new layer of copper atoms arriving on the strained copper film as caused by the increasing amounts of incorporated oxygen. Taking the slope of this line and dividing by the (111) biaxial modulus of copper (261 GPa) gives a lattice parameter strain of -1×10^{-5} per copper monolayer grown after oxygen consumption. Additional adlayers of copper deposited on the strained surface must also strain by the above quantity in order to maintain epitaxy. This epitaxially enforced strain is the mechanism by which further compressive stresses develop within the film.

5.5 Reversible Stress

Figure 5.6 presents reversible stresses observed upon halting of growth after complete incorporation of oxygen.

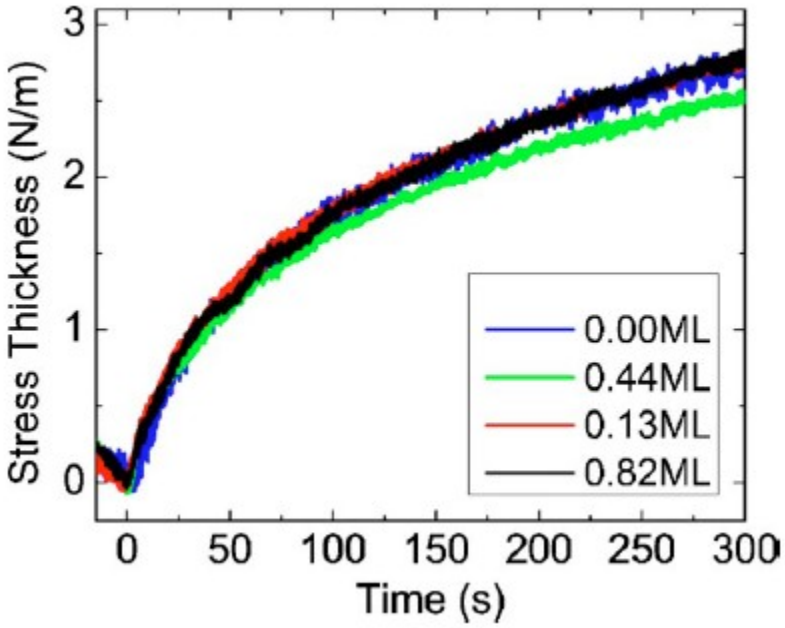

Figure 5.6. Plot of reversible stress after interruption of growth for various oxygen dosages. There does not appear to be any notable variation that is within experimental error. Reproduced with permission from (Kennedy 2007).

The zero point on the time axis corresponds to ceasing in growth after 250 Å of copper has been deposited after oxygen dosage. These growth cessations also occur after steady state has been reached, meaning that all effects of the Cu_2O islands have been completely occluded.

The results clearly show that the reversible stresses are unaffected by the Cu_2O islands buried within the bulk of the copper film. This is unsurprising, as the current models explaining reversible stresses involve either the surface or interaction between the surface and grain boundaries and have little dependance on the properties of the interior of the film.

5.6 Conclusion

In the above work, the effects of adsorbed oxygen on the growth of copper on a copper {111} surface were quantified. A model of slowly consumed oxygen floating on the growth surface was devised to explain the stress behavior of the system. Using this model and key features of the stress-thickness plots, several important details were extracted, such as the additional stress per added monolayer of oxygen and the lattice strain modification due to the incorporated oxygen.

Ideally, the information and research presented thus emphasizes the relationship between structure and stress, a subject for which the dissertation prospectus is to be approached. This relationship is revealed in a literature review of thin film stresses, where the differing stages of thin film growth morphology were shown to correlate to the stress evolution of the film. The relationship was again demonstrated by the work of oxygen on copper, as the modification of the structure of the copper due to the oxygen was directly observed in the stress evolution of the film. Next, work done on the adsorption of carbon monoxide on platinum {111} is presented. In this work the relationship of structure and stress, this time of the adsorbed carbon monoxide gas, will continue development.

CHAPTER 6

CARBON MONOXIDE AND PLATINUM

6.1 Introduction

The previous chapter described the change in continued growth stresses due to the adsorption of a gaseous species. A natural follow up question is what stresses are induced only by gaseous species? To answer this question the next work presented focuses on absorption of carbon monoxide on a platinum {111} surface. The reason for choosing this system, as opposed to oxygen on copper {111}, is the large amount of existing literature for the structure carbon monoxide adopts when adsorbed on a platinum {111} surface (Ogletree 1986, Blackman 1988, Steininger 1982, and Campbell 1980). This allows for proper interpretation of adsorption stresses which would be less facile in the less studied oxygen on copper {111} surface. From the literature on structure, links can be made between the structural evolution of the carbon monoxide adsorbate to the observed surface stress state of the system. A new parameter is also introduced, Φ, to help elucidate this correlation and define a key value in surface stress for adsorption. The study also required the development of a new type of stress monitor, without which proper examination of the adsorption stresses would be near impossible.

6.2 Experimental Details and the DSM

The experimental equipment used in this work is described previously in Chapter 5. One of the biggest differences is the use of a diaphragm based sensor as opposed to a cantilever type stress sensor. The inability to use a cantilever for

these types of experiments stems from how the cantilever type geometry would allow a gaseous species to adsorb to the back side of the substrate in addition to the surface of interest. Any stress results are then the difference between the stresses induced by carbon monoxide adsorption on either side of the cantilever and therefore erroneous. In order to only expose one side to the carbon monoxide gas, the geometry was switched to that of a diaphragm, where the curvature of the diaphragm is tracked with the same capacitance based sensor through deflection of the center-point. Calibration is done in the same manner as in Chapter 4, however eq 4.1 is replaced by eq 6.1 appropriate for a supported plate, shown below.

$$d = \frac{3\rho g r^4}{8 E_s t_s^{\,2}} \tag{6.1}$$

where ρ is the density of the diaphragm, g is the acceleration due to gravity, r is the radius of the diaphragm, E_s is the elastic modulus of the diaphragm, t_S is the thickness of the diaphragm, and d is the deflection at the center of the diaphragm. This is combined with the Stoney relation for a clamped disk

$$\Delta f = \frac{E_s t_s^{\,2} d}{3 r^2 (1-\nu)}$$

and results in a different calibration factor. In addition to a different calibration, a new device needed to be created in order to properly hold the diaphragm, isolate

one side of the diaphragm, and yet allow the isolated side to be evacuated to avoid a pressure induced curvature and additional stress measurement error. The design that met these criteria developed by the author is shown schematically below in Figure 6.1.

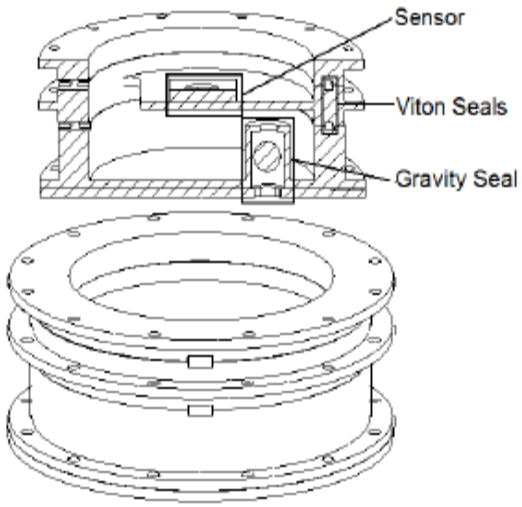

Figure 6.1. Schematic of the Diaphragm Stress Monitor, comprised of a flexible substrate (not shown), capacitance sensor, gravity seal, and three housing components. The housing components mate via Viton seals inserted in the marked channels. The flexible substrate is held between the upper pair of Viton seals and deflections are recorded by the sensor located directly below the center of the substrate. The gravity seal, when inverted, seals the inner volume so the impinging flux arrives only at the outer face of the substrate (Kennedy 2011).

This Diaphragm Stress Monitor (DSM) used Viton seals to softly clamp the substrate of borosilicate glass and create a negligibly leaky seal. The gravity seal

used a free floating ball bearing. When oriented substrate down, the ball seals an orifice and prevents gas flow into the interior of the DSM. This is critical as it prevents adsorption of carbon monoxide on the backside of the substrate. When oriented substrate up, the ball lands in a non-spherical orifice, allowing gas flow out of and into the interior of the DSM. This let the DSM reach UHV conditions both inside and outside the sensor so that no appreciable pressure induced deflections would occur. Calibration was achieved in a similar manner to the cantilever sensor by inverting the DSM and comparing the gravity induced deflection to output signal. The Pt substrate was prepared by sputter deposition. Initially a 1.5 nm chromium adhesion layer was sputter deposited on the 300 um borosilicate membrane. Upon this, the {111} textured platinum film was deposited, with texture verified via x-ray diffraction (XRD) after experimentation as seen is Figure 6.2 below.

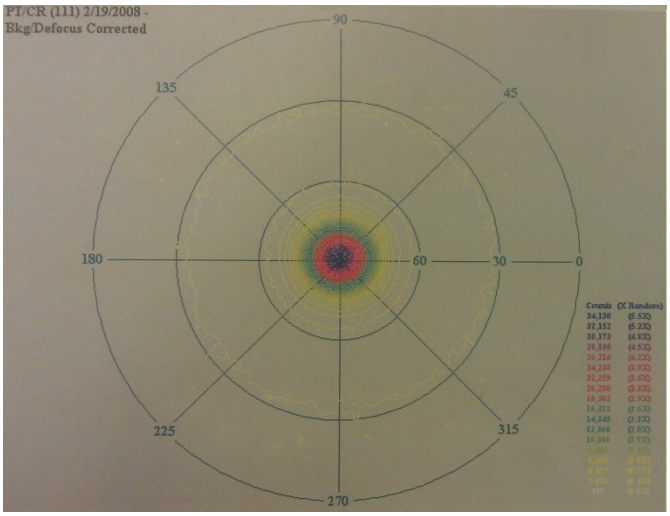

Figure 6.2. Pole plot of the X-ray count for the {222} diffraction angle. In plane angle defines the rotation of the sample, while radius from the center signifies tilt of the sample. The majority of the intensity being at the center of the plot signifies that a majority of the {111} planes are parallel to the substrate surface.

Ultra-high purity carbon monoxide (99.9%) was used as the leak in gas for adsorption through a sapphire seat leak valve. The quantity of carbon monoxide adsorbed was recorded on the same QCM used to record substrate surface preparation growth, ensuring a similar surface between the two. Two sets of six experiments were performed. The last four of each set were averaged to obtain the results. The reason for exclusion of the first two of each set was due to the lack of repeatability for those runs. They varied drastically, while the last four of each set were highly similar in magnitudes and features between both individual experiments and between the two sets. The variation of the first two runs is most likely attributable to outside contamination from introduction into vacuum and the repeated runs served to annihilate adsorbed contaminants.

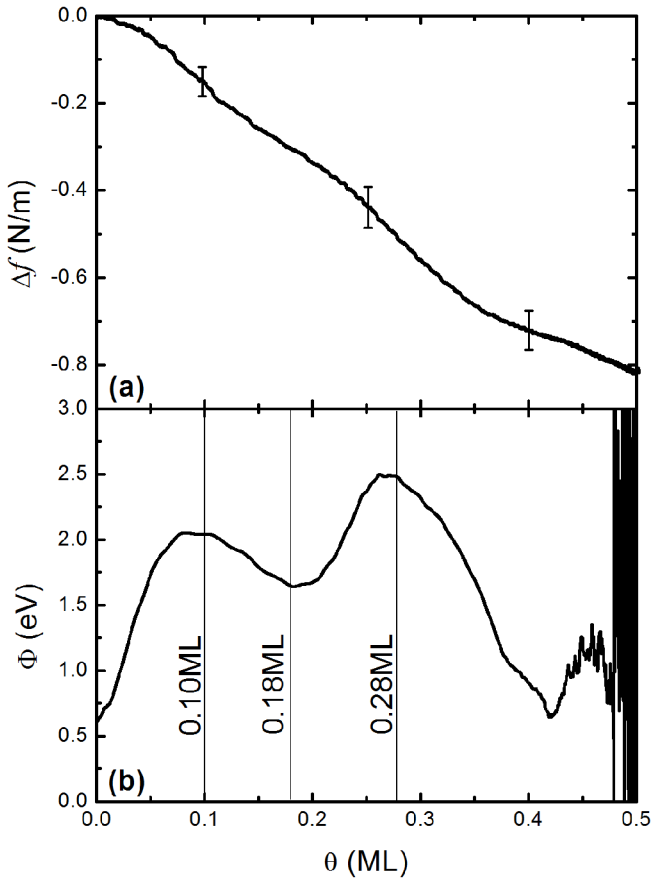

Figure 6.3. (a) Plot of change in surface stress vs. carbon monoxide coverage on a platinum {111}-textured thin film. The error bars at 0.1 ML, 0.25 ML, and 0.4 ML represent one standard deviation at the respective coverage. (b) Plot of $\Phi = -df/d\Theta$ versus coverage. Demarcations at 0.10 ML, 0.18 ML, and 0.28 ML correspond to carbon monoxide coverages at which structural changes in the adsorbate layer are known to occur (Kennedy 2011).

Figure 6.3a is the plot of the stress change versus carbon monoxide coverage, where 1 carbon monoxide monolayer is defined as a 1:1 ratio of carbon monoxide molecules to surface platinum atoms, from the averaged experiments detailed above. The plot is rather nondescript, and it is initially difficult to identify any features of significance. To alleviate this problem a new parameter, Φ, is introduced and defined as

$$\Phi = \frac{\delta f}{\delta \rho}$$

Figure 6.3b is the plot of Φ versus carbon monoxide coverage. It immediately becomes clearer where prominent changes in the surface stress behavior occur, and are demarcated by vertical lines. At the onset of adsorption, the initial value of Φ is representative of the stress change induced by the interaction of a single carbon monoxide molecule interacting with the platinum surface and only the platinum surface. If there was no direct carbon monoxide-carbon monoxide interaction or platinum surface mediated carbon monoxide-carbon monoxide interaction, we would expect Φ to remain a constant as there is no other term to change how the carbon monoxide interacts with the platinum surface. The plot shows, however, that even for marginal increases in the carbon monoxide coverage, a shift in the value of Φ is observed. This is indicative of interaction of the carbon monoxide molecules on the surface. The nature of this interaction is relatively uncertain, as it could be through space via electrostatic

forces, through the substrate via electronic effects, or through the substrate from force dipole interactions. The maxima of Φ at 0.1 ML is quite peculiar, as there has been no observed structural developments and only on-top (a carbon monoxide molecule directly above a platinum surface atom) sites are occupied at least until 0.18 ML (Steininger 1982). The most likely cause of this is a change of interaction mechanism, such as a shift from long range substrate mediated electronic interactions to short range through space electronic interactions (Einstein 1996). The change in Φ at 0.18 ML, however, has some experimentally observed structural attributes to account for the change at this coverage as seen in Figure 6.4a below.

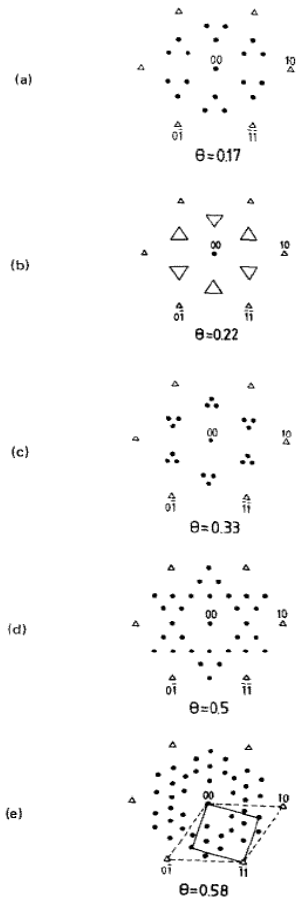

Figure 6.4. A schematic of the observed LEED patterns reproduced with permission from (Steininger 1982). The small triangles represent diffraction spots due to the platinum substrate, while the black dots represent diffraction spots due to the adsorbed carbon monoxide. The larger triangles represent diffuse diffraction spots. θ is the coverage of carbon monoxide in mono-layers where one mono-layer corresponds to a one-to-one ratio between adsorbed carbon monoxide molecules to surface platinum atoms.

0.18 ML has been reported as the onset of a non-trivial change in site occupancy. At this coverage bridge sites, those above the point between two platinum surface atoms, become occupied at the expense of on-top sites. This

provides a clear structural change associated with the change in surface stress behavior. A complication in this simple picture, however, arises from the observation of diffuse (√3x√3)R30 Low Energy Electron Diffraction (LEED) pattern that occurs at 0.22 ML (Steininger 1982). This structure reaches saturation at 0.33 ML, meaning that the diffuse pattern should correspond to islands of the (√3x√3)R30 LEED phase in conjunction with a disordered phase consisting of on-top sites and bridge sites, indicating attractive interactions.

At the coverage of 0.28 ML, where we see yet another change in Φ, the saturation coverage of the (√3x√3)R30 LEED structure occurs within experimental error. After 0.33 ML, the system begins to nucleate and transition to the c(4 x 2) phase (Steininger 1982). This phase consists of carbon monoxide arranged in a unit cell comprising two carbon monoxide molecules, one at a bridge site and one at an on-top site. This structure reaches saturation at 0.5 ML, which is also the saturation coverage of carbon monoxide (Campbell 1980).

At 0.5 ML, so near to saturation, a very large amount of time passes for a very small change in coverage. This arises from the reduction of both available adsorption sites and driving force for adsorption. Because of this large time period, the slight amount of drift and noise present, normally negligible, becomes amplified and results in the odd noise-like feature present in the derivative Φ. The wild changes are only the result of an experimental artifact and do not represent real changes in the system. They were included for completeness.

While there are well-defined structural changes associated with the observed changes in Φ, the nature of these changes also proves interesting. Generally, stability of non-close packed ordered structures is due to repulsive interactions between neighbors. However, the existence of these phases as islands within other phases leads to the conclusion that some form of attractive interactions also exist. The nature of these interactions could be attributed to indirect electronic interactions, as these are capable of sign change that oscillates with separation (Einstein 1973, Einstein 1996, and Roelofs 1996).

6.4 Conclusion

The above work consists of the adsorption of carbon monoxide on a platinum {111} surface utilizing a unique instrument, the DSM. The work shows the stress-structure correlation for the structural evolution of the carbon monoxide adsorbate and the surface stress evolution of the platinum {111} surface during this process.

CHAPTER 7

ICE THIN FILMS

7.1 Introduction

Water is a prevalent yet unusual substance. It has at least eleven stable crystalline forms and a wide variety of morphological motifs which can vary widely depending on such factors as temperature and pressure (Martin 2010). From the standpoint of scientific curiosity, the breadth of water's behavior makes it a prime candidate for study. The goal of this research is to establish a stress-structure relationship between the morphology of an ice film and the stresses that arise not only during its growth but also upon subsequent annealing. The focus of this work is on ultra-thin ice film growth temperatures below 160 K and in the UHV environment (less than 1 x 10^{-8} Torr background pressure), as it is under these conditions that other factors (e.g. contamination) are eliminated. Also, the growth of ice has been widely studied and is well-defined in terms of morphology and structure for these conditions. Water deposits either in crystalline hexagonal ice or amorphous ice at these experimental conditions (Delval 2004, Smith 1996, Brown 1996, Thürmer 2008, Zondlo 1997, Spisa 2001 and Haq 2002). The combination of well-defined growth structure, elimination of adverse factors, and precise control of the ice growth will allow for a more clear interpretation of results and facilitate the correlation between stress and structure.

7.2 Determining Factors for Ice Thin Film Structure

Of first concern are the determining factors between amorphous and crystalline ice growth. Amorphous ice is in a non-equilibrium state due to its higher free energy than hexagonal ice. Thus, deposition of amorphous ice from the vapor phase is the result of purely kinetic factors, the first of which is growth rate, which is directly related to the partial pressure of water vapor (Brown 1996). This relationship is governed by the kinetic law of gases, shown in eq 7.1

$$J_{H_2O} = \frac{P_{H_2O}}{\sqrt{2\pi k_b T_{H_2O}}}$$
$$Rate = \frac{J_{H_2O} m_{H_2O}}{\rho_{ice}} \qquad (7.1)$$

where J is the incoming molecular flux, P is the partial pressure, m is the mass of the molecule, k_b is the Boltzmann constant, T is the temperature of the vapor, and ρ is the density. The rate calculated from eq 7.1 assumes a capture efficiency of unity which has proven reasonable for these temperatures and pressures (Brown 1996). The importance of growth rate and its impact on morphology is a result of the difference between bulk and surface diffusion. Bulk diffusion is slower than surface diffusion for ice (Brown and George 1996). Thus, the longer a molecule remains as a surface molecule the more likely it is that it will diffuse to a crystalline configuration. If the growth rate is high, the time period during which the molecule is on the surface lessens and the film is likely to become amorphous as a result. The second factor affecting growth crystallinity is the temperature of

the substrate upon which the ice is deposited due to molecular motion induced by increased temperature. A warmer substrate causes more motion and it becomes more likely that the film will adopt the equilibrium crystalline morphology under these conditions. Most of the literature presented fixes the growth rate at approximately 1 nm/s and varies the growth temperature, as the temperature seems to have a greater effect on morphology than growth rate (Delval 2004, Smith 1996, Brown 1996, Thürmer 2008, Zondlo 1997, Spisa 2001 and Haq 2002). At this growth rate, the transition between amorphous and crystalline growth occurs at approximately 120 K, with amorphous growth below, and crystalline growth above, the transition. While the bulk growth phase is determined by a transition temperature of 120 K, both amorphous and crystalline phases begin growth with a wetting layer.

7.3 Wetting Layer

The growth of a wetting layer on FCC (Face Centered Cubic) {111} type systems generally begins with the creation of hexamers from the alignment of individual water molecules. A hexamer is a group of six water molecules forming a ring of hexagonal symmetry (Verdaguer 2006). These hexamers tend to stretch the intermolecular oxygen-oxygen bond in water to maintain registry with the substrate at on-top sites, but will generally not compress to fit lattices with shorter inter-atomic spacings (Verdaguer 2006). The tendency for the hexamers to stretch but not compress leads to varying degrees of registry depending on the substrate. Also, water tends to congregate around step ledges of the substrate as seen in Figure 7.1a below.

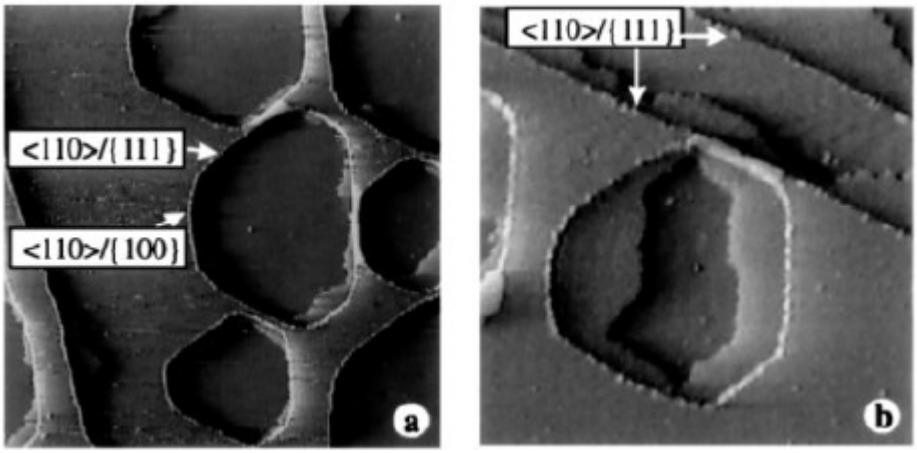

Figure 7.1. STM image of Pt(111) with water adsorbed on the surface. A 2-D water layer is observed developing inside the lower terrace. Image originally from Morgenstern M. et al. (1996), Phys. Rev. Lett. 77, 703. Copyright 1996 by the American Physical Society.

Depending on water-substrate interactions, continued growth can result in the propagation of a coherent layer as seen in Figure 7.1b or in 1-D like chains as seen in Figure 7.2.

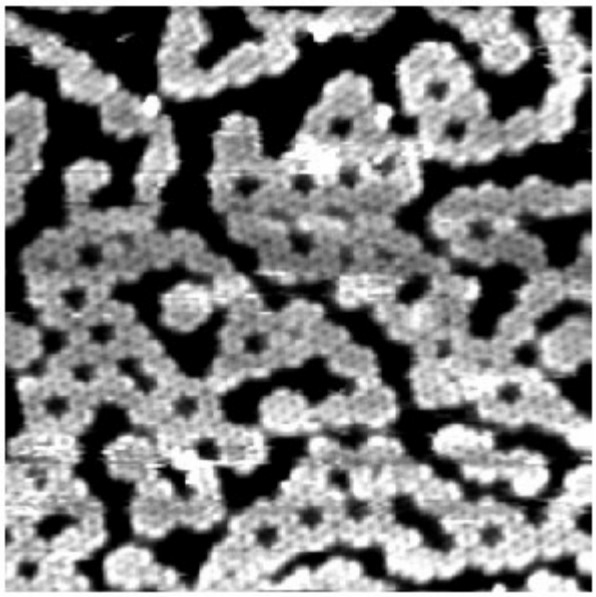

Figure 7.2. STM image of D2O on Pd(111) at 100K that details the chainlike growth of hexagonal “honeycombs”. From Cerda J. et al. (2004), Phys. Rev. Lett. 93, 116101. Copyright 2004 by the American Physical Society.

The wetting layer eventually coalesces into a complete layer that is hexagonal in nature (Verdaguer 2006). The 2-D hexagonal structure of the wetting layer is reasonably well established from several studies, but the 3-D structure of this layer is not well understood and several models have been proposed (Michaelides 2003). Figure 7.3 is a collection of several structural possibilities.

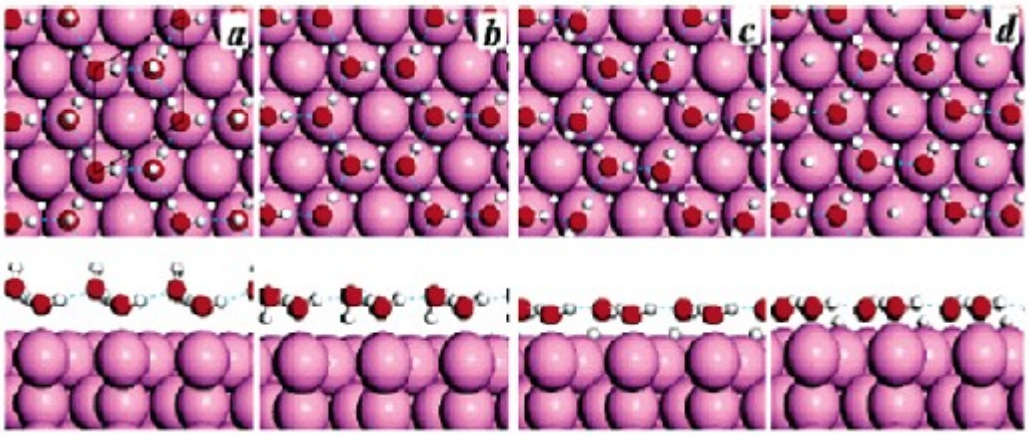

Figure 7.3. 3-D structures that have been proposed for water's wetting layer. (a) and (b) are a H up and down configuration respectively. In these configurations, hydrogens are shared between each oxygen forming hydrogen bonds. Excess hydrogen not participating in this bonding is either located above an oxygen and pointing out (a) or is located between oxygen and the underlying substrate (b). (c) shows a transition state for dissociation, where the excess hydrogen is shown partially dissociated from the oxygen, and (d) shows a dissociated water layer where the excess hydrogen is fully dissociated and occupies an unoccupied above site. Reprinted with permission from Michaelides A. et al. (2003), J. Am. Chem. Soc. 125, 2746. Copyright 2003 American Chemical Society.

While the exact nature and structure of the wetting layer is not known, significant progress has been made in the study of its behavior and in understanding of the growth of ice past the initial wetting layer.

7.4 Bulk Ice Thin Film Growth

The work by K. Thürmer and N. C. Bartelt provides detailed visuals of the growth of both amorphous and crystalline ice on platinum (111). Figure 7.4 shows the morphology of a developing amorphous film.

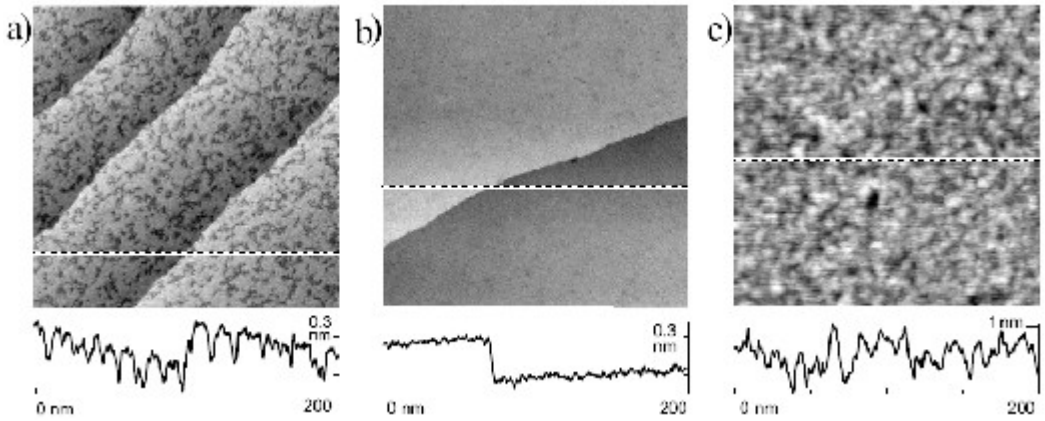

Figure 7.4. 200 nm x 200 nm image of ice growth at 100 K (amorphous). Thicknesses are 1.7, 2, and 20 bilayers for image (a), (b), and (c) respectively. From Thürmer K. and Bartelt N. C. (2008), Phys. Rev. B 77, 195425. Copyright 2008 by the American Physical Society.

Part (a) of the figure shows a film that is 1.7 bilayers (BL) thick. The "bilayer" notation for thickness (1 BL = 3.7 Å) comes from the propensity of ice to grow only in 2 molecular layer increments. In Figure 7.4a, the film exhibits a near constant upper bound in thickness, with sizable jumps from the step ledges of the underlying platinum (111) terraces and is characteristic of layer-by-layer type growth mode. Between Figure 7.4a and Figure 7.4b a change in roughness is observed, corresponding to a transition from an incomplete bilayer (1.7 BL) to a complete bilayer (2 BL). Continued growth results in Figure 7.4c at 20 BL and a

complete loss of the smooth nature of a layer-by-layer growth mode. The conclusion to draw from this behavior is that the layer-by-layer mode is a result of interaction between the ice film and the substrate. Once there is significant distance between the ice surface and the substrate, the driving force for a smooth layer-by-layer film diminishes and the film is free to take on the porous, rough surface seen in Figure 7.4c. The images above provide a general reference for the growth of amorphous ice. With differing substrates, features such as the upper thickness limit of layer-by-layer growth may change, but the core behavior is similar (Doering 1982, Thürmer 2008, and Brown 1996). Because amorphous ice is highly sensitive to kinetic considerations, changes in growth temperature and rate (partial pressure of water) result in morphology changes, which are mostly seen in the evolution of porosity, or amount of excess surface per mass of ice deposited. Several studies, using such techniques as FTIR (Fourier Transform Infra-Red spectroscopy) (Zondlo 1997 and Spisa 2001) and refraction measurements (Brown 1996), establish a trend of increasing growth rate and decreasing temperature that cause an increase in excess surface and a decrease in density in the amorphous ice film. This result shows that as the system becomes more kinetically limited the ice has diminished ability to eliminate the excess surface. Removing kinetic limitations (that is, creating conditions of ample thermal energy and time), results in denser and less porous ice. The limiting case in this situation is the transition to crystalline ice.

Figure 7.5 is a series of images showing the evolution of a crystalline ice film during growth.

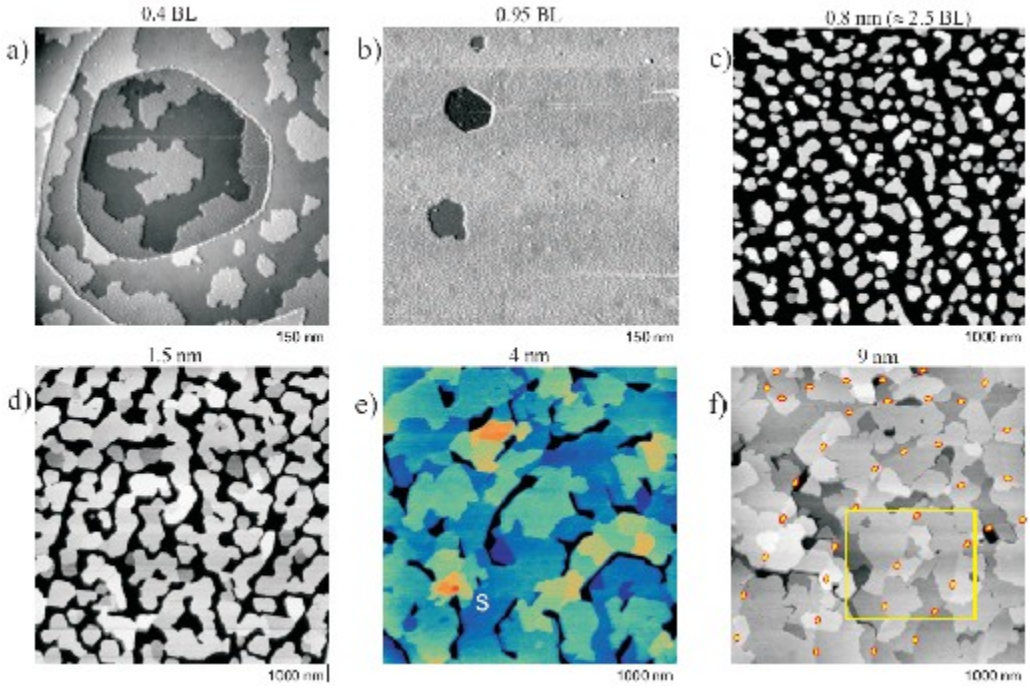

Figure 7.5. STM images of the various growth stages of crystalline ice. Growth is at 140 K. From Thürmer K. and Bartelt N. C. (2008), Phys. Rev. B 77, 195425. Copyright 2008 by the American Physical Society.

Figure 7.5a is taken of an ice film at a thickness of 0.4 BL and shows repetition of the phenomena in Figure 7.1 for the development of the wetting layer. In Figure 7.5b at 0.95 BL the wetting layer is observed at near completion with a somewhat smooth, single-layer structure. In Figure 7.5c (at approximately 2.5 BL) the formation of the first "true" ice crystallites is seen. These crystallites are about 2 to 3 nm in height and are embedded in the wetting layer of water, still present in the black regions of the image. Figure 7.5d is taken at 1.5 nm of ice growth and

shows coalescence of the crystallites which continues in Figure 7.5e. Finally, bulk crystalline ice growth is observed in Figure 7.5f at 9 nm. In total, the growth of crystalline ice on platinum (111) exhibits features similar to SK type growth observed in metal thin film deposition as discussed earlier.

7.5 Experimental Details for Ice Thin Film Growth

The structure information presented above will be combined with the results from the experiments below to give a full picture of the ice thin film system. To begin discussion of the experimental details, we focus on the chamber in which these experiments were conducted, shown schematically in Figure 7.6.

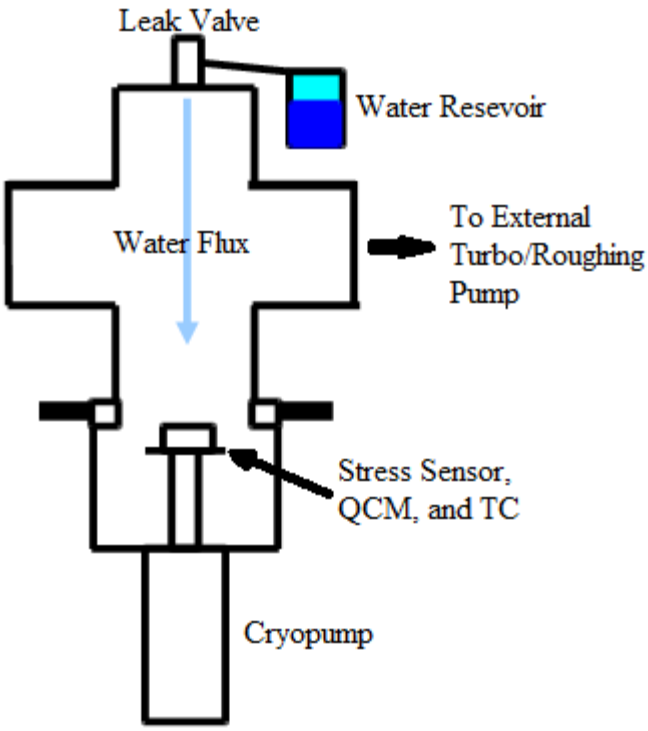

Figure 7.6. Simple schematic of the vacuum chamber used in the ice thin film experiments.

Figure 7.6 is a simplified schematic of the vacuum chamber used to perform the stress measurement experiments. Initial pumping to approximately 5 x 10^{-7} Torr is performed through the combined work of a turbo-molecular pump and a diaphragm roughing pump. Further pumping to 5 x 10^{-9} Torr is accomplished with a cryopump located at the bottom of the chamber. Sample heating and chamber bake-out are done with a quartz lamp. Water partial pressures are induced and controlled using a sapphire seat leak valve located at the top of the chamber with an accuracy of 1 x 10^{-8} Torr. Base and partial pressures of water are measured using a standard ion gauge. Stress measurements are performed using a customized capacitance based cantilever sensor that is capable of repeated cycling between < 75 K and 298 K. The cantilever's polycrystalline copper is approximately 250 um thick. Copper was chosen to promote thermal conduction and maintain a uniform temperature. Calibration of the stress sensor is performed by the gravity inversion technique covered in Chapter 5. Temperature is measured via a thermocouple gauge in contact with the stress sensor. Quantities of water absorbed are measured with a QCM, which is also in contact with the stress sensor to ensure high thermal conduction and nominally identical temperatures. A sample of the raw QCM data is presented in Figure 7.7.

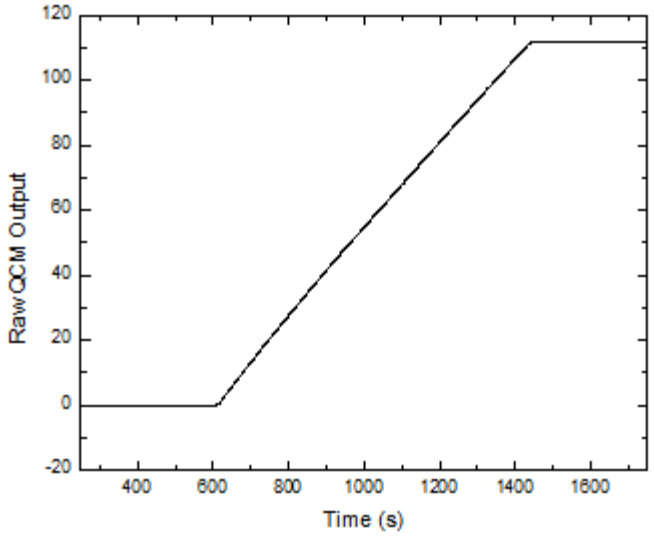

Figure 7.7. This figure is a representative plot of the raw QCM output. The adsorption of water begins at approximately 600 seconds and ends shortly after 1400 seconds. The data shows stable behavior before and after exposure to water vapor and simple linear behavior during exposure.

The QCM is calibrated by comparing output signal to the expected growth rates calculated from eq 7.1. The entire ensemble of QCM, thermocouple, and stress sensor is affixed to a cryopump for cooling.

The experimental procedure for the forthcoming results is as follows. First, the chamber and all devices are heated with a quartz lamp to assist in purging the system of residual water and contaminants. Next, the sample is allowed to cool for 12 or more hours to ensure a stable and homogenous temperature. As a consequence of this long cooling time and the finite water partial pressure in the system, an existing ice film collects on the surface of the

cantilever. Thus, all ice films grown are grown on ice as opposed to the substrate. Following the cooling period, approximately 10 minutes of drift data is recorded, after which the leak valve is opened and a partial pressure of water at 5×10^{-6} Torr is introduced. Data is recorded for approximately 12 minutes of ice growth, corresponding to about 500 nm of ice, at which point growth is halted.

Before continuing on to the results, there are several aspects of the experiments that proved challenging and are worthy of note. The first is the sapphire seat leak valve. This device required controlled heating, where the aperture of the valve was at an elevated temperature relative to the water reservoir. Without this heating, water will condense on the seat and result in "spitting" of water in the chamber. This causes uncontrollable spikes in water pressure and prevents a precise deposition rate.

The stress sensor itself also requires careful construction. The sensor originally used to obtain the earlier oxygen and copper results used a special type of solder to connect the wire and sensor head. Due to thermal cycling, the disparate thermal expansion coefficients result in mechanical failure of the interconnect. In order to surmount this problem, a purpose built sensor head was created by the author. Of critical importance in this device is the connection of the sense wire to the sense pad, and proper shielding. For the connection, a mechanical clamp was used to maintain conduction, but was insufficient as even slight increases in resistivity can alter the output signal. To alleviate this problem, gold leaf was applied as an additional interconnect between the sense wire and sense pad. This helped ensure that the contact resistance remained negligible.

The shielding was done by depositing gold on a kapton film and ensconcing critical exposed components. Kapton was used to keep the shielding insulated from the rest of the apparatus, as shorting would result in the loss of any meaningful signal.

The use of a cryopump as a cryostat results is one of the few reliable ways to create a controlled, low temperature environment. Originally, a flow-through chiller concept using a dry ice and acetone bath was attempted but ultimately failed. The logistics of pumping chilled acetone into vacuum without leaks and thermal loss proved insurmountable with the equipment available.

A final concern is the adsorption of ice onto the opposing side of the cantilever. If this were to occur, the stress signal of the experimental surface would be canceled out by the stresses developing on the backside. It is for this reason that the entire stress measurement apparatus is chilled to cryogenic temperatures. With the entire apparatus chilled, all water vapor condenses on and is trapped at the exposed surfaces, preventing vapor from reflecting off and allowing only line-of-sight deposition. The back of the cantilever is then simply kept out of line-of-sight and ensures no significant deposition occurs on the back.

7.6 Stress Results for Ice Thin Film Growth

Figure 7.8 below contains the collected results of several of these experiments over a range of temperatures.

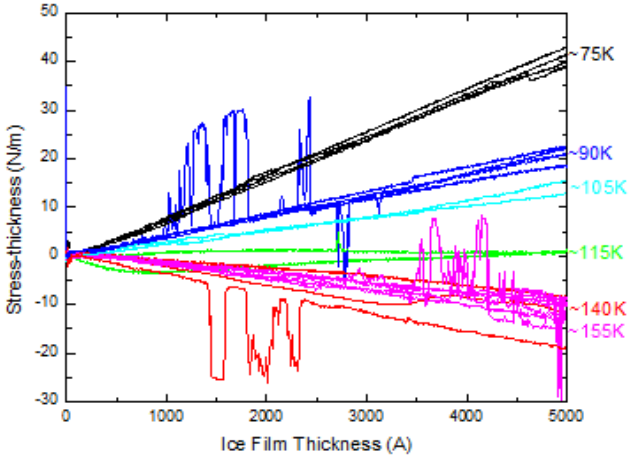

Figure 7.8. Collected data from several experiments for the growth of ice at various temperatures. Growth rate was held constant for a partial pressure of water at 5 x 10^{-6} Torr. Temperature groups include 75 K (black), 90 K (dark blue), 105 K (cyan), 115 K (green), 140 K (red), and 155 K (magenta). The jogs in the data are attributed to the significant vibration emanating from the cryopump.

Extracted from this data is a grouping of stresses that is based on temperature. At the coldest temperatures of 75 K, 90 K, and 105 K the stresses are tensile, with the lowest temperatures resulting in the highest tensile stresses. At 115 K the magnitude of the stresses is not distinctly tensile or compressive.

At higher temperatures of 140 K and 150 K the stresses become compressive, although there is no significant difference between the stress values at these temperatures. An explanation of these stresses may be found in the structures given in the literature.

Ice forms an amorphous porous phase at temperatures below 120 K and transitions to crystalline growth above 120 K. As seen in Figure 25, below 120 K a tensile stress develops, at 115 K the system experiences a transition in stress behavior, and above 120 K a compressive stress develops. This observation leads to the conclusion that amorphous growth generates tensile stresses and crystalline growth generates compressive stresses. There are probable explanations that link the observed stresses to the concomitant structure.

7.7 Explanation of Crystalline Ice's Compressive Stress

Compressive crystalline growth may be explained by invoking similar arguments that are used to explain compressive stress generation in continuous metallic thin films (Mays 1968, Koch 1994, Floro 2001, Chason 2002, and Friesen 2002). However, these arguments remain only speculation until the same experiments that support them in the metallic thin film cases are also performed for crystalline ice. Also, note that between 140 K and 155 K there is no significant change in compressive stress. This is reasonable for crystalline growth, where the kinetics is rapid enough that equilibrium structures are obtained in both the 140 K and 155 K cases.

7.8 Explanation of Amorphous Ice's Tensile Stress Due to Excess Surface Area

The amorphous films as-grown are highly porous, and the tensile stress may arise from the excess surface area that is associated with porosity. It is known that surface stress is tensile in nature (Shuttleworth 1950). As a porous film has a higher surface area compared to a planar surface, the total tensile stress is expected to be greater because of the greater available area for it to act upon. When the temperature is lowered to between 90 K and 75 K, studies using FTIR and optical interference measurements find a decrease in ice density and an increase in surface area (Brown 1996, Zondlo 1997, and Spisa 2001). The results in Figure 7.8 for temperatures of 90 K and 75 K show an increase in tensile stress when the growth temperature is lowered. The increase in surface area and tensile stress that occurs upon a decrease in temperature supports the conclusion that the tensile stresses are due to the tensile surface stress associated with a free surface.

A simple calculation can determine if the above conclusion is reasonable. In order to conduct this calculation, we would consider a simple cylindrical void through the thickness of the 500 nm thick ice film. For the pore size, we can estimate a reasonable pore diameter from the STM image in Figure 7.4. For the purposes of this calculation we will assume a diameter of 7 nm. Each pore then has a certain volume of solid ice associated with it. From the density of the ice film from FTIR and refraction measurements at 100K (Brown 1996), we can infer how much ice is associated with an individual pore and establish a "unit cell" for this calculation. The stress that the pore must create within the ice film can be extracted from the experimental results in Figure 7.8, which is 15N/m.

Through the use of all this information the required surface stress of the pore is calculated. We can then see if this value of surface stress is reasonable and comment on the viability of surface stress resulting in the observed stresses for the amorphous growth case.

7.9 Calculation of Stress Induced by Surface Stress Acting on a Pore

The geometry for the unit cell of this calculation is that of two concentric columns, where the inner column is the pore, and the material between the inner and outer columns is ice as seen in Figure 7.9 below.

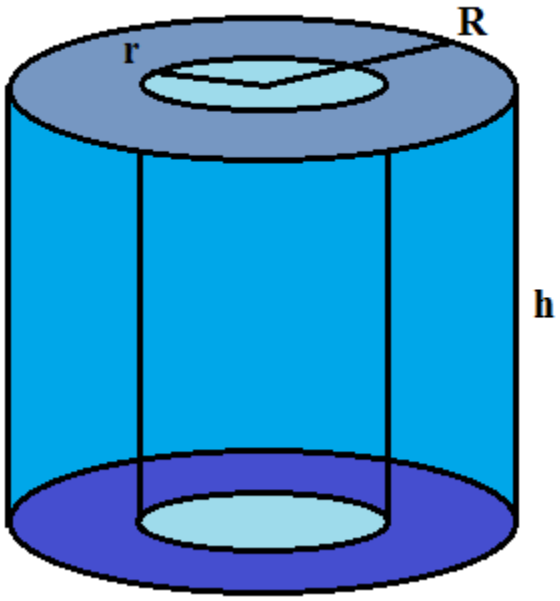

Figure 7.9. Shows the concentric columnar unit cell geometry to be considered for calculation. *R* is the total radius of the cell, *r* is the radius of the pore, and *h* is the thickness of the film.

From this geometry the volume of the pore, *v*, is calculated as

$$v = \pi r^2 h \tag{7.2}$$

and for a radius of 3.5 nm and a height of 500 nm the pore volume is 1.924 x 10^{-23} m^3. Referring to (Brown 1996) we note the bulk density of ice is 0.9 g/cm^3 and the density of ice grown at 100 K is approximately 0.83 g/cm^3. The volume of void space relative to the volume of ice is related to the densities as

$$voidfraction = \frac{\rho_{crystalline} - \rho_{amorphous}}{\rho_{crystalline}}$$
$$V = \frac{v}{voidfraction} \tag{7.3}$$

where ρ is the density of the respective phase, *v* is the pore volume calculated earlier, and *V* is the unit cell volume. This allows for determination of the cell volume in the unit cell which is 2.474 x 10^{-22} m^3 and has a total radius of 1.255 x 10^{-8} m. With the dimensions of the unit cell defined, the next step is to set up a force balance equation between the surface stress within the pore driving the closure of the pore in balance with the elastic stresses within the ice resisting closure. Both arguments are related to a small change in *r*, Δ*r*. The surface stress term is

$$F_{pore} = 2\pi fh\Delta r \tag{7.4}$$

where F_{pore} is the driving force for closure of the pore, f is the surface stress of ice, and h is the thickness of the film. Note that the driving force is simply the reduction of pore surface area and its associated surface stress. For the elastic stresses in the ice, this is calculated as the stresses acting on the area of the pore as

$$\begin{aligned} F_{elastic} &= \sigma A_{pore} \Delta r \\ F_{elastic} &= \sigma 2\pi r h \Delta r \end{aligned} \tag{7.5}$$

where $F_{elastic}$ is the mitigating force of straining the ice, σ is the stress in the ice, A_{pore} is the area of the pore that σ is acting upon, r is the radius of the pore, and h is the thickness of the film. σ is calculated by taking the film force measured in Figure 7.8 and dividing it by the film thickness h. In order for the system to be in equilibrium the forces must balance and therefore are equitable, resulting in

$$\begin{aligned} F_{elastic} &= F_{pore} \\ \sigma 2\pi r h \Delta r &= 2\pi f h \Delta r \\ \sigma r &= f \end{aligned} \tag{7.6}$$

Using the values for σ and r, we obtain f = 0.105 N/m, which is a reasonable value for surface stress. Since this value is of order the normal values seen for surface stresses of real materials (Haiss 2001), it is reasonable to state that the tensile stresses induced during amorphous growth are due to surface stresses acting on the excess surface area of the pores. A natural counter argument is that

the calculated *f* is perhaps too small. The response to this argument is that the model used in this calculation was set up to give both simplicity and maximum effect of the surface stress of the pore creating elastic stresses in the film. The real system is not that of columnar pores normal to the surface and is instead far more complex. The pores are also of non-uniform size and can be in different orientations relative to the substrate. These factors would lower the efficacy of the surface stress inducing bulk stresses, and increase the required surface stress necessary to induce the bulk stresses observed through the experiment.

7.10 Explanation of Amorphous Ice's Tensile Stress Due to Molecular Effects

One final mechanism that could be invoked to explain the tensile stress development utilizes the formation of the amorphous structure and polar nature of the ice. We can imagine that as an additional water molecule adsorbs on an existing ice film, the molecule interacts with several of its neighboring atoms. In a crystalline system, the arrangement of the molecules is such that there is good alignment between several molecules and their poles to produce a low energy structure. However, due to the kinetic limitations present during amorphous growth the molecules cannot diffuse to this low energy structure. Instead, it is quite reasonable that the amorphous system would strain to approach the low energy structure. This straining could then be the tensile stress observed in the data. This proposed mechanism is shown in a simplified manner in Figure 7.10.

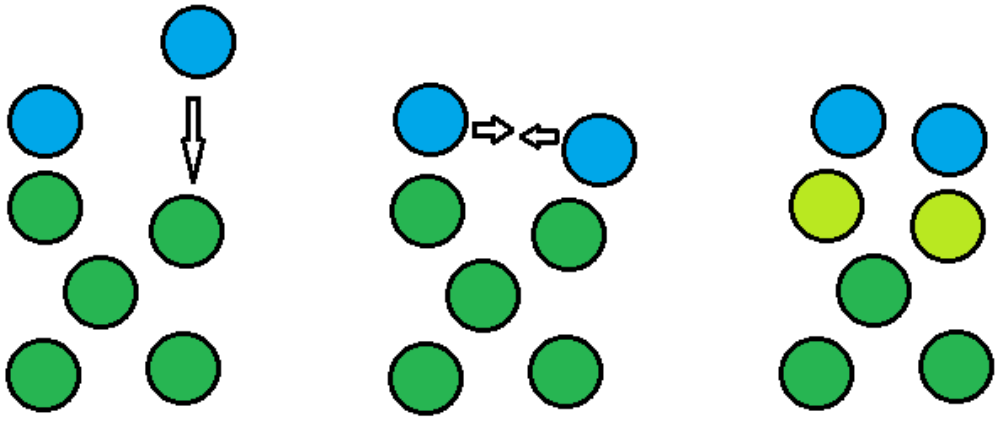

Figure 7.10. Simple schematic showing how a growing amorphous film could generate strain by the attractive forces between newly arriving molecules.

In order to account for the increase in tensile stress associated with a lower growth temperature, diffusion arguments can again be invoked. For the warmer amorphous growth there would be a greater fraction of water molecules that could diffuse to favorable or semi-favorable locations, reducing the number of water molecules contributing to the reconfiguration-strain induced tensile stress. At the lower temperatures, diffusion is further limited, and more molecules participate in the straining to obtain semi-favorable structures.

7.11 Introduction to Annealing of Ice Thin Films

Thus far the structure and stresses of a growing ice film from literature and from experimental results, respectively, have been discussed and theory linking the two presented. In order to gain further insight into this system, attempts to induce structural changes in an existing ice film and record the stress changes associated with the structural change were desirable.

One of the most straightforward methods to do this is through the heating and annealing of an amorphous ice film into a crystalline ice film. There is literature on this subject which can pulled from to confirm the viability of this induced structural transition.

Experiments were performed by Smith et al. where an amorphous ice film was heated after growth and sublimation fluxes were recorded (Smith 1996). The results of that study are reproduced in Figure 7.11.

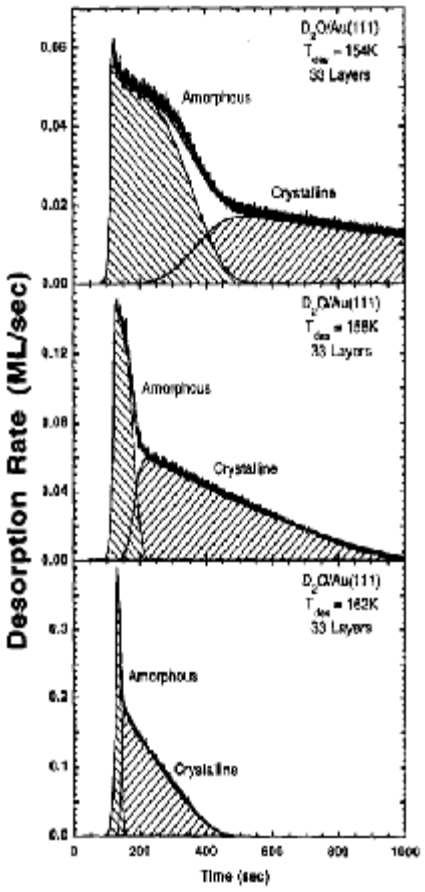

Figure 7.11. Desorption rate versus time for three temperatures for D_2O on Au(111). The shaded regions denote where amorphous or crystalline characteristic desorption rates are present. Reproduced with permission from (Smith 1996).

The heating experiment allowed the researchers to observe the transition from amorphous to crystalline ice as the structure changed in real time. The sublimation fluxes represent the structure that is present due to the relative instability of water in amorphous versus crystalline ice. A water molecule in amorphous ice is not as strongly bound to its neighbors as water in crystalline ice.

Thus, a smaller energy is required for sublimation of amorphous ice and results in higher sublimation rates relative to crystalline sublimation rates. This phenomenon is reflected in Figure 7.11 and allows inspection of the structural transition. However, measuring the stress changes associated with this transition is far from trivial.

7.12 Experimental Details for Annealing of Ice Thin Films

The experimental setup for the heating experiments is identical to that of the growth experiments. The protocol is also identical, except for two factors. First, the previous cryo-pump failed and required replacement with a different cryo-pump. Second, after growth the system is allowed to rest for > 30 min after which radiative heating is conducted through the use of the quartz bake-out lamp mentioned earlier. Heating was controlled with the use of variable AC voltage transformer (regulating United States standard 110V single phase power) set at 50% or 100% for a duration of either 20, 40, 80, or 120 seconds depending on the experiment. The system was allowed to relax for several hours after the heating event. Three sets of experiments were done. The first was for a growth temperature of approximately 145 K in the crystalline regime to serve as a baseline to compare against coupled with repeated 20 second heating events at 50% voltage. The second consisted of amorphous growth below 75K, and repeated 20 second heating events also at 50% voltage. The third set was also for amorphous growth below 75K, however, the heating events were stepped up to 40, 80, and 120 second successive exposures at 100% voltage.

For the 120 second exposure at 100% voltage the radiation was high enough to notice a significant heating of the chamber walls. This relatively high level of heating was done in order to guarantee that the sample was heated well above that needed for annealing.

An individual run is shown in Figure 7.12.

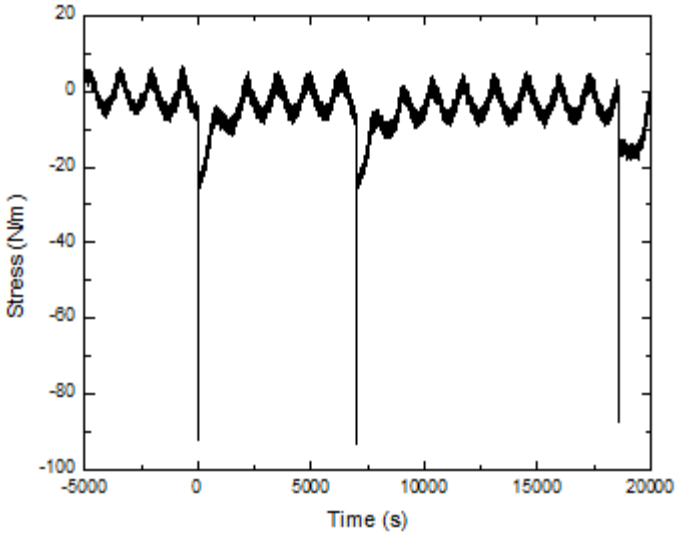

Figure 7.12. Individual heating experiment for an ice film growth at 145 K. Shows a periodic sinusoidal wave. Origin is most likely a 10 degree fluctuation observed on the cryo-pump cold head temperature.

First to note is how the 20 second heating event appears as a sharp spike in the data. This gives a qualitative scale for the time it takes for the system to reach equilibrium after the heating event. The purpose of the short burst of heating is so that a large flux, but low total heat, is introduced to the cantilever. This should result in a large temperature increase localized at the ice film, but once the heat

diffuses into the substrate and reaches equilibrium the overall temperature is not significantly increased. If the overall temperature were to increase, there would be an erroneous thermal signal convoluted with the stress associated with any film structural changes. Also of note is the periodic modulation of the stress signal. This is due to a periodic temperature change in the cyropump that was used as a cryostat. The period sine wave character of each individual run was troubling, and if possible it would be advantageous to identify and eliminate its source. To do this both the ambient temperature and cooling water temperature,

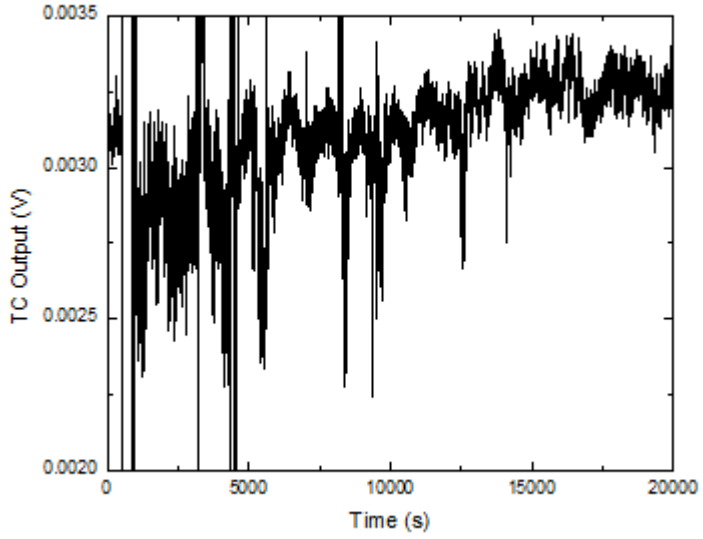

Figure 7.13. Plot of the output of a thermocouple measuring the ambient temperature around the chamber. A slight modulation is recorded but lacks the consistency of the sinusoidal wave recorded in the stress results.

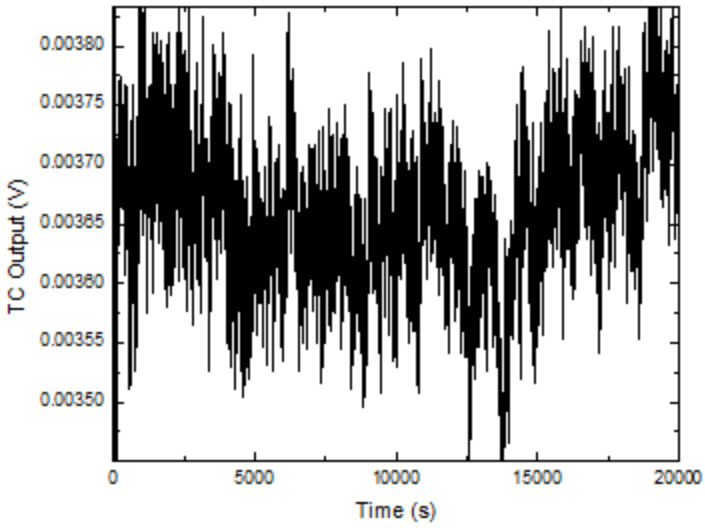

Figure 7.14. Plot of the output of a thermocouple measuring the temperature of the cooling water line for the cryo-pump compressor. This lacks the clear periodic signature seen in the stress results.

were tracked with a thermocouple. From Figure 7.13 and Figure 7.14, no clear sinusoidal wave is observed, though in Figure 7.13 there is some modulation. This means that the fluctuation is internal to the cryopump and not readily fixed. The solution to surmount the noise was then to perform multiple runs and average out the wave as best as possible.

7.13 Annealing Crystalline Ice

Figure 7.15 shows the stress results from repeatedly annealing a crystalline film for 20 seconds at 50% voltage. The time axis was zeroed at the start of the first heating event, so that the flat region before zero time corresponds to the > 30 minutes rest period. Later downward spikes reaching the x axis correspond to

subsequent heating events. The stress state at the rest period was selected as the zero point for the stress axis so that all stress results are changes relative to the rest state. This zeroing protocol is consistent for all heating results presented.

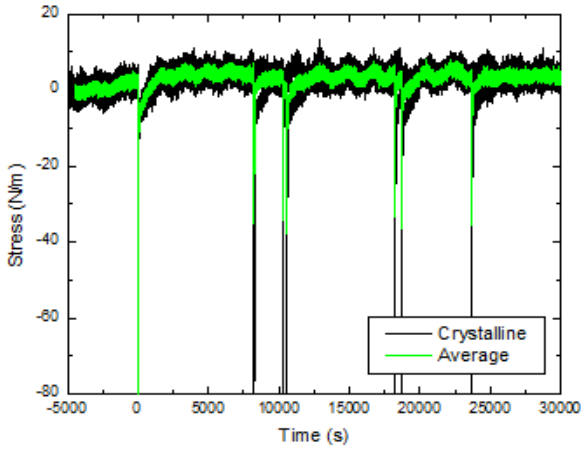

Figure 7.15. Shows the results from several experiments conducted at a sample growth temperature of 145 K. Individual runs are in black while the average is in green. The later heating events do not align in time between each run; however, they show that subsequent heating events do not induce stress changes.

As for the stress change of interest, it is the overall stress change between the relaxed state and the stress state after the system reaches equilibrium. The magnitude of the overall stress change is quite small, of order 4 N/m in the tensile direction taken from the average at 0 seconds and 5000 seconds. This is reasonable for a crystalline film as this structure is stable and annealing would introduce only small structural changes.

The tensile shift when the crystalline ice film is annealed could have several possible sources. Recalling the results for the growth of a crystalline ice film from Figure 7.8, there is a built-in compressive stress within the film. If this stress is partially annealed out of the film, the relaxation of a compressive stress would look identical to the introduction of a tensile stress and could account for the observed tensile stress. Another possibility is from thermal expansion effects. If the ice film is heated sufficiently, all the existing stresses within the film could be annealed out. However, since the film is at an elevated temperature, the lattice parameter of the crystalline ice is larger than at its original temperature. Thus, as the film cools back down the film would tend to undergo thermal contraction, but due to the traction with the substrate it would develop the observed tensile stress instead. A final possibility is that the crystalline film, which is poly-crystalline, is undergoing densification through Ostwald ripening (Ostwald 1887). This densification would naturally result in the film tending to contract, but due to traction would instead result in a tensile stress. This leaves us with three viable paths in which the crystalline ice film could develop the observed tensile stress as related to its structure (annealing of a compressive stress, thermal contraction stress, or Ostwald Ripening).

7.14 Annealing Amorphous Ice with Insufficient Heating

Figure 7.16 contains the results from the heating of amorphous ice for 20 seconds at 50% voltage.

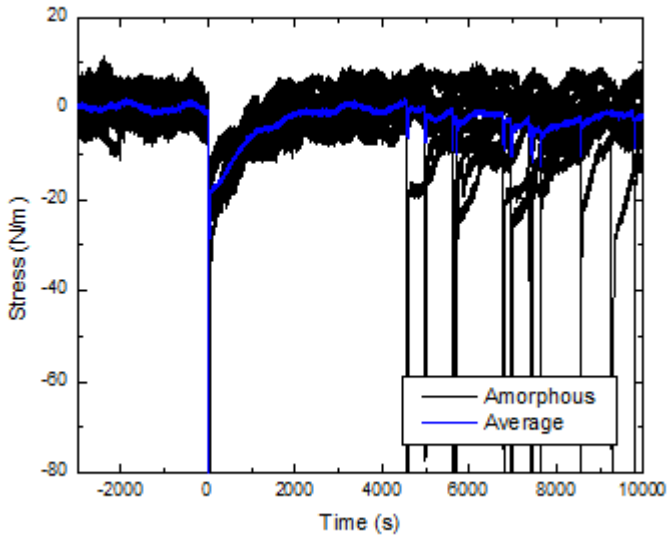

Figure 7.16. Plot of amorphous ice films grown below 75 K and heated for 20s at 50% voltage. Individual runs are plotted in black and the average plotted in blue. Later heating events are not aligned in time and thus pull down the average stress.

Note that the stress change associated with annealing is also almost zero within experimental error. This is a curious result, as some sort of change associated with the heating would be expected. This prompted an increase the heating and conducting a third set of experiments.

7.15 Annealing Amorphous Ice with Sufficient Heating

Figure 7.17 contains the results from the third set of experiments where the heating was stepped from 40 to 80 to 120 seconds at 100% voltage.

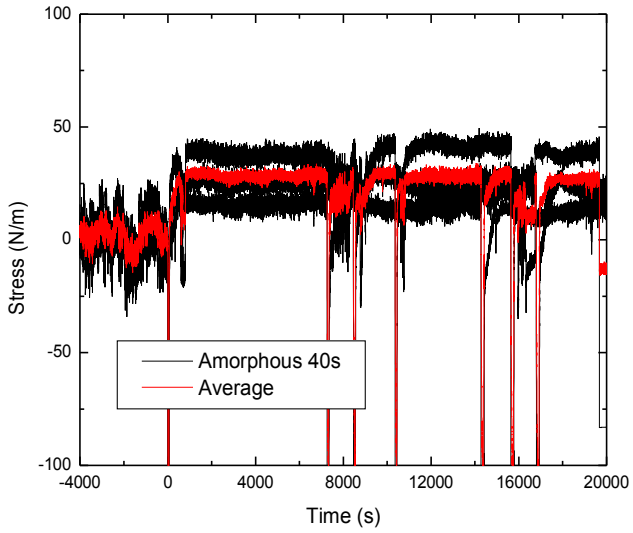

Figure 7.17. Plot of several amorphous ice films grown below 75 K and heated for 40 seconds, 80 seconds, and 120 seconds. The zero time was centered at the 40 second heating event. The latter spikes in the data reaching the x axis are subsequent heating events for 80 or 120 seconds. An average is shown in red.

A significant tensile stress change exists at the 40 second heating event. The tensile stress change of approximately 29 N/m (once again taken between 0 and 5000 seconds) is significantly larger than the crystalline results from Figure 7.15.

There are several possible explanations that could be used to account for the large tensile shift upon annealing of the amorphous film. The first argument that should be brought up is that this greater tensile rise simply corresponds to the greater heating done on the film and a greater thermal contraction upon cooling. This would be valid until consideration is given to the subsequent heating events. These events are larger than the heating event associated with the tensile stress change and yet result in no net stress change. If the anneal/thermal contraction mechanism were active we would expect a further increase in tensile stress, which is not observed. Another mechanism that would be a viable explanation is the densification of the film through either one of two paths. The annihilation of the pores found within the amorphous ice film, or the density increase associated with conversion from the looser amorphous molecular arrangement to the tighter and denser crystalline arrangement.

To begin we'll consider the pore argument. If pore annihilation is indeed the cause of the tensile shift during annealing, then this result would significantly call into question the growth tensile stresses being caused by surface stress acting on excess surface area. Elimination of the pores would remove the excess area in which the surface stress was acting, which should result in a compressive stress that is not observed. This is unless the tensile stress due to densification is large enough to overwhelm the compressive relaxation. This is quite possible, as the density difference between amorphous and crystalline morphologies is of order 7%. The ideal strain from conversion of these two structures is calculated as

$$\sigma = \varepsilon M_f \tag{7.7}$$

where σ is the ideal stress from pore closure, ε is the ideal strain from pore closure, and M_f is the biaxial modulus of ice. Multiplying this strain by the biaxial modulus of ice (14.5 GPa (Petrovic 2003)) we obtain a stress value of 1.015 x 10^9 Pa, which corresponds to a stress thickness for a 500 nm film of 507 N/m. As this value is significantly larger than the observed tensile stresses, it is reasonable to argue that the pore annihilation and excess surface area arguments remain valid. It should be noted however that plastic deformation or cracking would occur at these stresses without the relaxation provided by diffusion.

The other densification argument involves the conversion of the less dense amorphous molecular structure to the denser crystalline molecular structure. This conclusion would, like the previous mechanism, call into question a tensile growth stress mechanism. In this case it is the argument of restructure-strain induced tensile stress during growth. In order to increase the amorphous films density to that of crystalline, the tensile stress associated with the amorphous structure should be required to anneal out. Once again both these mechanisms could be active if the tensile rise due to density increases outweighs that of the compressive relaxation. However, in this case it is more difficult to calculate if this is reasonable, as the dominant majority of the lower density in the amorphous film is due to pore void space as opposed to the disordered amorphous structure.

In order to ultimately determine the active mechanisms in both the growth stresses and annealing stresses, further structural studies would need to be done that are currently not in literature at the time of the writing of this dissertation. Such works would include STM imaging of a pre- and post-anneal crystalline ice film similar to that seen in Figure 7.4. Additional work via Transmission Electron Microscopy (TEM) could also be used to track the structure of the amorphous ice after annealing and inspect the strain induced due to crystallization.

7.16 Characterization of the Heating Event

Up to this point consideration has only been given to the stress difference between the original state of the as-grown film and after the film has been allowed to reach equilibrium after annealing. If possible it would be beneficial to characterize the behavior of the stress response during relaxation and attribute it to some process occurring within the system.

Earlier, it was argued that the heating was done in a short, intense burst so that there would be a high localized temperature increase to anneal the film at the surface, but after diffusion the total temperature increase would be negligible to avoid thermal expansion error. Following this rationale, the transient within the stress response after heating should be attributable to the diffusion of the heat through the substrate and the non-uniform thermal expansion within the sample. If this is indeed the cause of the stress transient, it should be possible to model this phenomenon and calculate an anticipated curvature response. If the curvature response corresponds with the experimental transient it is then reasonable to conclude that the transient is indeed caused by the thermal expansion.

The scenario proposed is shown in Figure 7.18 below.

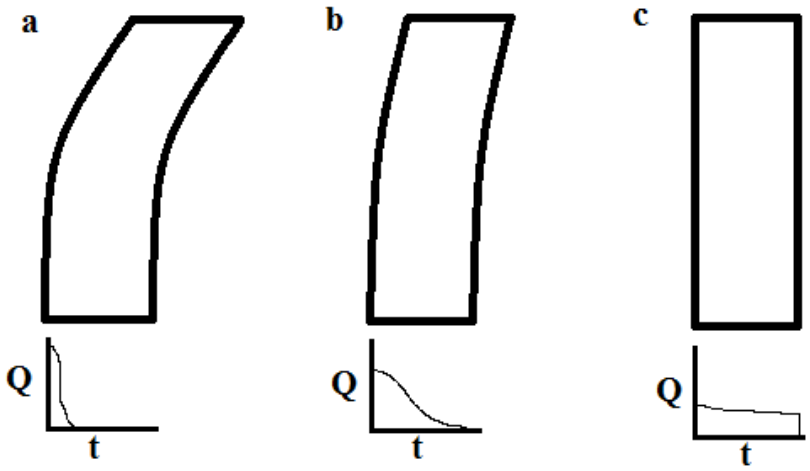

Figure 7.18. Simple cartoon showing the concept of cantilever curvature as time progresses (from a to c) and heat is allowed to diffuse from the left surface to the interior of the cantilever. The plot below each cantilever shows the heat concentration Q as a function of the depth into the cantilever t. The heat starts highly concentrated at the left side, and due to thermal expansion effects induces the cantilever to bend to the right. Progressing to the image at the right side of the figure, the heat diffuses and becomes balanced on either side of the cantilever, resulting in no net bending.

The heat is assumed to be localized in an infinitesimally thin layer at the surface of the substrate. This is both a good assumption in that it is reasonably valid for the experimental setup, as the heating even of 20 seconds is short compared to the relaxation time of around 2500 seconds, but it also has a closed form solution to the diffusion equation (Crank 1975).

$$Q = \frac{m}{\sqrt{\pi Dt}} e^{\frac{-x^2}{4Dt}} \tag{7.8}$$

where Q is the concentration of heat at a given depth and time, m is the total amount of heat initially at the surface of the substrate, D is the thermal diffusion constant of the substrate, t is the time that has passed, and x is the depth from the surface. This equation gives the heat concentration at any depth within the substrate relative to time. Since the cantilever is copper, the heat concentration is converted into a local temperature by the specific heat, s, and density of copper, ρ. Finally this is then converted to a local thermal strain via α, the coefficient of thermal expansion at 100 K (Simmons 1957). The end strain state at a given depth and time is then

$$\frac{m\alpha}{\sqrt{s\rho}} e^{\frac{-\left(\frac{h}{2}-z\right)^2}{4Dt}} \tag{7.9}$$

where s is the specific heat of copper at 100 K, α is the coefficient of thermal expansion of copper at 100K, ρ is the density of copper, and z is the distance from the cantilever midplane (the switch in co-ordinate system was done to facilitate the energetics calculations). In order to calculate a curvature for a cantilever subject to these effects, we refer back to the energy minimization technique presented in Chapter 3, where the local energy strain energy density is given in eq 3.2. We add to this the strain from the thermal expansion effects to give an energy

density function U,

$$U = M_s\left(\varepsilon_o - \kappa z - \frac{\alpha Q}{s\rho}\right)^2 \tag{7.10}$$

Mirroring the original energy minimization technique, we integrate U through the thickness of the substrate, giving a total energy V of

$$\begin{aligned} V = M_s\left(\varepsilon_o{}^2 h + \frac{h^3\kappa^2}{12} - \frac{4\alpha\kappa m\sqrt{Dt}}{s\rho\sqrt{\pi}} + \frac{4\alpha e^{\frac{-h^2}{4Dt}}\kappa m\sqrt{Dt}}{s\rho\sqrt{\pi}}\right) \\ -M_s\left(\frac{\alpha\sqrt{D}(2\varepsilon_o - h\kappa)m\sqrt{t}\,Erf\left[\frac{h}{\sqrt{2Dt}}\right]}{s\rho\sqrt{Dt}} - \frac{\alpha^2 m^2\,Erf\left[\frac{h}{\sqrt{2Dt}}\right]}{\sqrt{2\pi Dt}(s\rho)^2}\right) \end{aligned} \tag{7.11}$$

where *Erf* [ ] is the error function of the argument in brackets. Note that we want to simultaneously minimize the total energy V with respect to the extensional term ε_o and the curvature κ term. Looking at eq 7.11, this is not feasible to do analytically due to the presence of the error function. However, it is straightforward to accomplish numerically via a mathematics software suite such as Mathematica.

For this calculation discrete time points were selected and input, after which the software minimized the energy function relative to the two aforementioned terms. A screen capture of one such calculation is shown in Figure 7.18.

In[41]:= `V = Integrate[U, {z, ((-h) / 2), (h / 2)}]`

Out[41]=
$$Ms\left(eo^2\,h+\frac{h^3\,k^2}{12}-\frac{4\,a\,k\,m\,\sqrt{d\,t}}{\sqrt{\pi}}+\frac{4\,a\,e^{-\frac{h^2}{4\,d\,t}}\,k\,m\,\sqrt{d\,t}}{\sqrt{\pi}}-\frac{a\,\sqrt{d}\ (2\,eo-h\,k)\,m\,\sqrt{t}\ \text{Erf}\left[\frac{h}{2\sqrt{d}\,\sqrt{t}}\right]}{\sqrt{d\,t}}+\frac{a^2\,m^2\,\text{Erf}\left[\frac{h}{\sqrt{2}\,\sqrt{d}\,\sqrt{t}}\right]}{\sqrt{d}\,\sqrt{2\,\pi}\,\sqrt{t}}\right)$$

In[273]:=
```
m = 82.724
Ms = 208*10^(9)
a = 2.87099*10^(-12)
d = 1.1234*10^(-4)
h = 225*10^(-6)
t = 2000
```

Out[273]= 82.724

Out[274]= 208 000 000 000

Out[275]= 2.87099×10^{-12}

Out[276]= 0.00011234

Out[277]= $\frac{9}{40\,000}$

Out[278]= 2000

In[279]:= `Minimize[V, {k, eo}]`

Out[279]= $\{-1.22251\times10^{-27}, \{k\to-4.87943\times10^{-14}, eo\to2.82687\times10^{-10}\}\}$

Figure 7.19. Screen capture of one of the numerical minimization calculations of the energy function *V* with respect to the arguments k (κ) and eo (ε_o). The constant a is the coefficient of thermal expansion of copper divided by the density and specific heat of copper. The constant m is the initial amount of heat and was approximated to be 83 J/m^2 based on the maximum deflection during the heating event.

The value of M_s was calculated as 208 GPa, α as 7.7 x 10^{-6}, s as 300 J/kgK, D as 1.1234 x 10^{-4} m^2/s, and the copper cantilever thickness h as 225um (Simmons 1957, Marquardt 2000, and Ledbetter 1987). Note that the total heat introduced, m, is a considerable source of possible error, but only in the absolute magnitude of the curvature result and should have no significant effect on the shape and temporal behavior. The calculation was also done for m equal to 1 J/m^2 and retained the same behavior. The resultant curvature value was then tabulated along with its associated time and plotted. In order to correct for the earlier mentioned error associated with the assumed total heat, an arbitrary scaling factor was used to scale the calculated curvature values to the experimental stress transients. An independent scaling factor was applied to each of the 3 sets of experiments to fit the thermal model to them. This is shown in the following 3 figures.

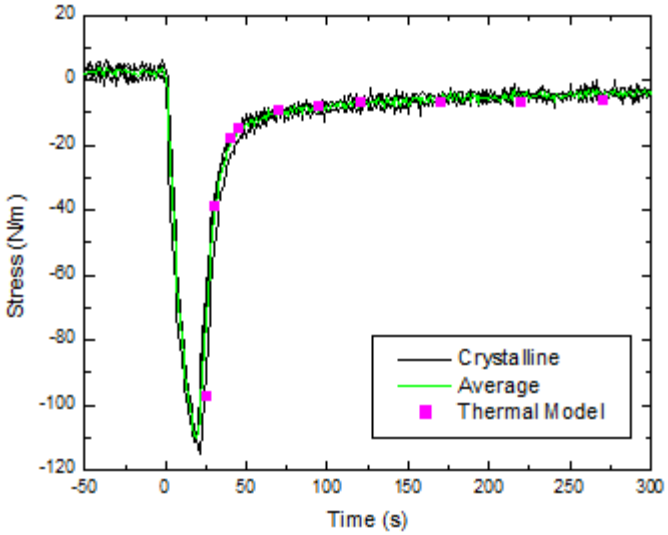

Figure 7.20. Shows a close-up of the heating event data for the crystalline sample set heated for 20 seconds at 50% voltage. The individual runs are in black, the average in green, and the scaled thermal model in magenta squares.

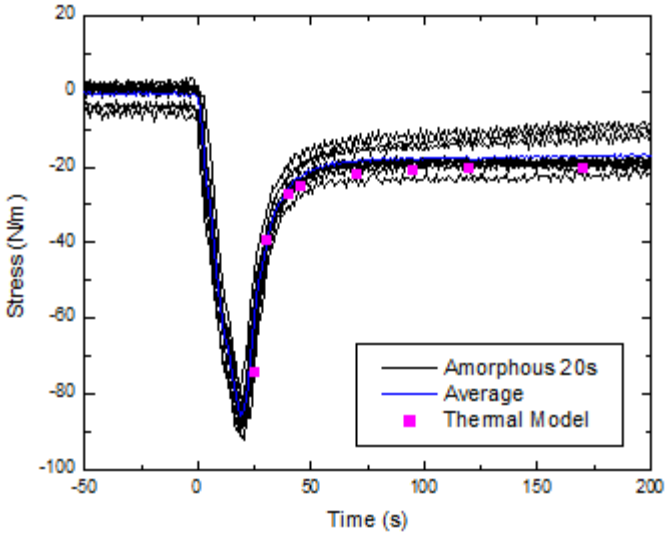

Figure 7.21. Shows a close-up of the heating event data for the amorphous sample set heated for 20 seconds at 50% voltage. The individual runs are in black, the average in blue, and the scaled thermal model in magenta squares.

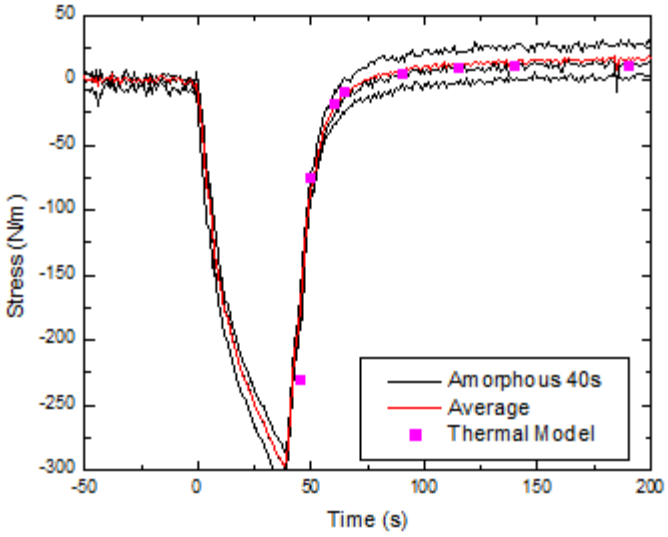

Figure 7.22. Shows the event stress data for the amorphous sample set heated for 40 seconds at 100% voltage. Individual runs are shown in black, the average in red, and the scaled thermal model in magenta squares.

The calculated curvatures, with only the application of a scaling factor, mirror the experimental stress transient quite well. From this, the conclusion that the stress transient is dominantly due to the thermal expansion associated with the diffusion of heat through the substrate is strongly supported. This then means that the physical changes in the ice film should occur quickly and then remain stable.

Another calculation of value is to back-calculate the amount of heat imparted to the sample by the quartz lamp. This is done by inspection of the amount of thermal stress in the cantilever and the heat required to generate this stress through thermal expansion effects. While it is complex to properly account for the diffusion of heat into the sample without introducing an arbitrary scaling factor, it is possible to circumvent thermal diffusion by inspecting the slope of the stress curves at the onset of heating and obtain an approximation of the heating rate from the lamp.

To simplify the calculation, all the heat imparted to the cantilever is assumed to occupy only a 100nm thick "film", valid only since the calculation is utilizing the slope of the stress curve at very early times. The thermally induced stress is then calculated as below.

$$-\delta f = \frac{M_s \alpha h_f \delta H}{\rho s}$$

In eq 7.12, δf is the slope of the stress curves found in Figure 7.20 and Figure 7.21 taken at 0 seconds, M_s is the biaxial modulus of copper at 100 K (201.5 GPa), α is the thermal expansion coefficient of copper at 100 K (7.7×10^{-6} / K), h_f is the assumed film thickness of 100 nm, δH is the thermal energy increase per unit volume of heated material, ρ is the density of copper, and s is the specific heat of copper at 100 K (300 J / kg K) (Simmons 1957, Marquardt 2000, and Ledbetter 1987). From Figure 7.20 and Figure 7.21, the slopes for 50 % and 100 % heating

are -5.922 N / m s and -16.551 N / m s respectively. Using eq 7.12 yields a volumetric heating rate of 1.024 x 10^8 J / m^3 s and 2.861 x 10^8 J / m^3 s for the 50 % and 100 % heating cases, respectively. This is converted into a heat flux by multiplying by the assumed film thickness h_f, giving 10.24 J / m^2 s and 28.61 J / m^2 s respectively.

It may be possible to extract from the heating event the actual behavior of the stress of the annealing film by subtracting out both the linear component from the radiative heat flux and the relaxation induced by the heat diffusing into the cantilever. Both of these quantities have been calculated or modeled already, so it should be straightforward to do so. To avoid complication the analysis will be performed on two individual runs run as opposed to the average.

The first step would be to subtract the linear component from the 40 second heating event as seen in Figure 7.22, which was calculated earlier as 16.551 N / m s. This then yields Figure 7.23 below.

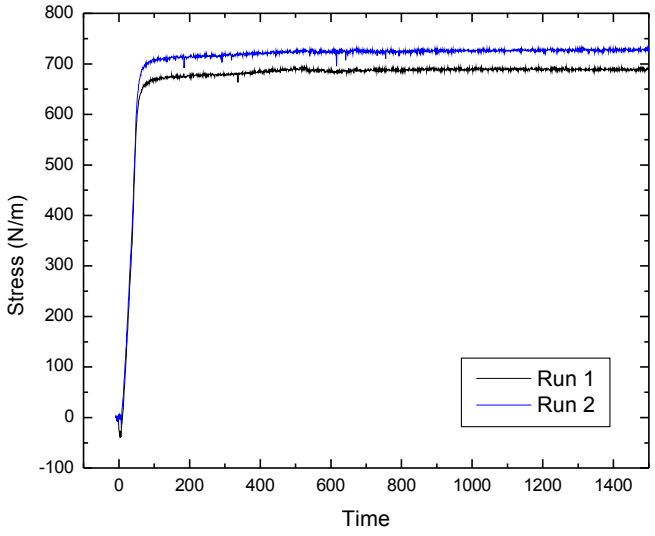

Figure 7.23 showing the curvature of the cantilever as a function of time with the linear effect of the radiant heat flux removed.

Originally it would be desirable to subtract the heat diffusion model as is. However, an assumption of the model is that the original heat is constrained to a very thin layer, and thus could not be extended into the heating event. This constraint can be circumvented by utilizing the additive property of diffusion (Crank 1975). This is done by taking the model, reducing the magnitude of curvature relaxed by 1 / 40th of the total curvature needed to be relaxed, and then repeating the model 40 times with each instance of the model shifted 1 second forward with respect to the previous. Conceptually, what is occurring is that each single second of flux is being collected in an infinitesimal layer at the surface, retaining the assumptions of the model, and being relaxed out independently.

The end result is the aggregate of each of the 40 1 second heating events. This new aggregate model is then plotted alongside Figure 7.23 as seen in Figure 7.24 below.

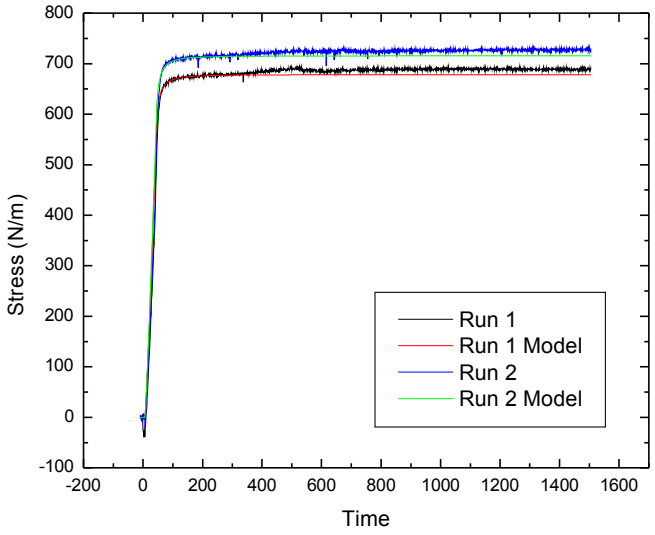

Figure 7.24 showing the aggregate model plotted alongside the curvature behavior from Figure 7.23.

Note that the aggregate model follows the linearly corrected curvature data quite well. It is now possible to subtract the aggregate model from the linearly corrected curvature data without risk of significant deviance from the assumptions inherent in the original model. This results in Figure 7.25.

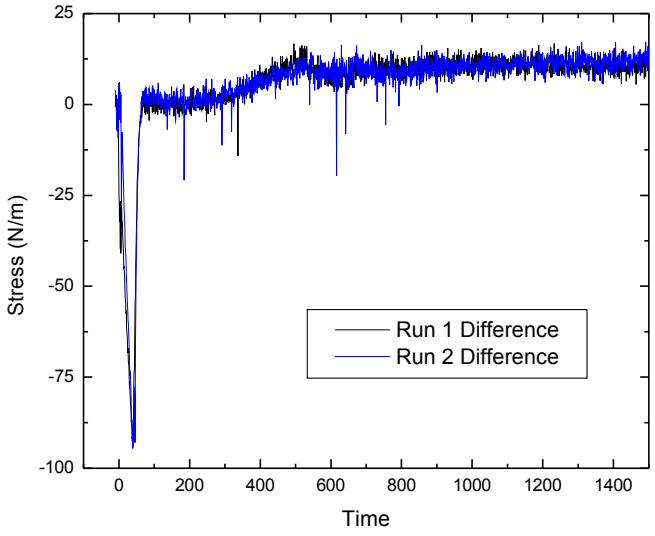

Figure 7.25 showing the difference between the linearly corrected curvature data and the aggregate model.

Ideally Figure 7.25 would show the behavior of the annealing ice film, which is supported in that both plots from separate runs are strikingly similar. The plot also has some peculiar features though that are unexpected. The first is the linear region from 0 to 40 seconds. The first thought that comes to mind is that the region is some error from the linear correction of the radiant flux. This is not the case. If that additional slope is added into the linear correction, the aggregate model would also then require an increase in magnitude to still fit the linearly corrected data. This increase in magnitude of the aggregate model offsets the correction of the linearly corrected data and the net effect is that the linear region in Figure 7.25 is preserved. Since it is likely not an error from the linear

correction, another reasonable interpretation is that the linear region is associated with the ice layer having a different coefficient of thermal expansion relative to the copper substrate. As both material heat, the disparate coefficients could easily cause the observed stress, which is of order -2.5 N / m s. After the 40 second heating even there is a rapid relaxation followed by a long term region. The rapid relaxation region is similar to the behavior of the thermal diffusion model, however appears to be of a much shorter timescale. This could be interpreted as heat diffusing away from the ice layer specifically, although this is conjecture. What is of significant interest is the long term region where in both runs there is a somewhat linear tensile shift between 250 seconds and 500 seconds. It is this region that is most likely entirely attributable to the annealing of amorphous ice to crystalline and as such it is prudent to perform an avrami analysis on this region

Figure 7.26 is the data from Figure 7.25 plotted as the ln (ln (1 / f)) versus ln (time) where the minimum and maximum values of f were scaled to be 0 and 1 respectively. The results are shown below.

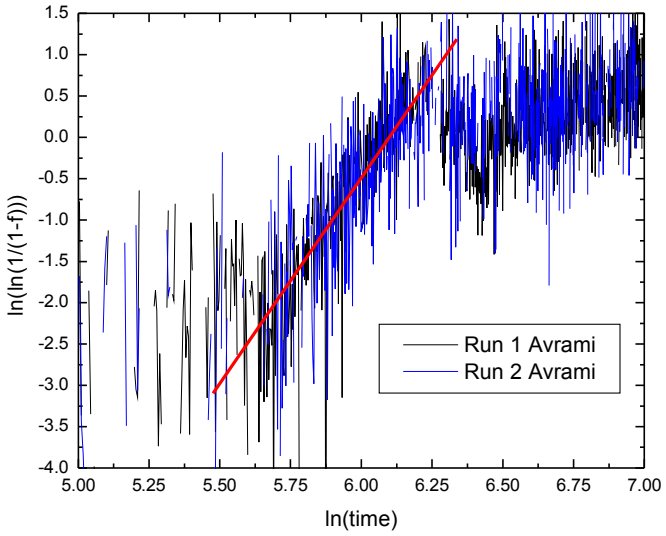

Figure 7.26 shows the data from Figure 7.25 plotted in a manner appropriate for an Avrami analysis where the vertical axis is plotted as ln (ln ($1/f$)) and the horizontal axis is plotted as ln (time). The red line indicates where the slope for the calculation of n was taken.

From Figure 7.26 the Avrami constant n can be taken. This value was calculated as 4.96. The physical interpretation is somewhat difficult and speculative. Generally, each integer value of n corresponds to an increase in the dimensionality in the phase change growth or nucleation. For n = 4 this is typically interpreted as 3D growth with random nucleation. The transition to n = 5 for this system is therefore puzzling. It is possible that the increase in n accounts for heat diffusing from the copper cantilever into the ice layer.

This is possible as a dominant majority of the radiative heat flux could pass through the ice and instead only be absorbed by the copper cantilever. The heat would then only be introduced to the ice via linear diffusion which could increase n from 4 to 5 as observed.

While a significant amount of information has been garnered from the works presented in this dissertation, there will always be additional research that could be conducted in order to further the understanding of the systems explored. This thought naturally leads to consideration of what additional research would be prudent to conduct in the future and how it would be accomplished.

CHAPTER 8

FUTURE WORKS

8.1 Introduction to the Future Works

This chapter will cover future works that would serve to further the understanding of the systems presented in Chapters 5, 6, and 7. As such, the proposed works will begin with those associated with the oxygen on copper work presented in Chapter 5, then the carbon monoxide on platinum {111} research presented in Chapter 6, and finally end with possible experiments developing the ice thin film growth presented in Chapter 7.

8.2 Future Works for Oxygen on Copper

The research conducted on the effects of a sub-monolayer of adsorbed oxygen on the continued growth of a copper surface proved quite insightful. However, as is the nature of science, there is always room for further study. Two possible experimental venues would prove very valuable. The first would be to determine if the oxygen incorporates itself into the grain boundaries or the bulk of the growing copper film. The second would consist of mirroring the carbon monoxide on platinum {111} work to determine the adsorption stresses of oxygen on copper {111}.

To determine the incorporation site of oxygen in growing copper, a reasonable method would be either the use of a highly sensitive elemental mapping technique like Auger Electron Spectroscopy or the use of a single crystal copper substrate. Auger analysis would, if sensitive enough to the miniscule amount of oxygen present, provide a 2D map of the oxygen concentration. A high

density at the grain boundaries would prove incorporation into the grain boundaries during growth. But, as the oxygen coverage is so small, it would be far more prudent to use a single crystal cantilever and repeat the oxygen-dosed growth experiments. By eliminating the presence of grain boundaries through a single crystal substrate, the importance of grain boundaries in the oxygen incorporation can be determined. If the stress behavior is different than the poly-crystalline case, then the conclusion would be that the oxygen is incorporated into the grain boundaries. Conversely, if no appreciable difference is recorded in the stress signal then the oxygen is trapped in the bulk of the film as it grows. The challenge with a single crystal experiment lies in obtaining a single crystal large enough and of appropriate geometry.

In addition to the incorporation site of oxygen during continued copper growth, it would also be valuable to use the DSM to measure the adsorption stresses of oxygen on a copper {111} surface. This proposed work, however, would be done as more of an exploratory experiment, as there is not as much literature on the structure of oxygen on copper {111} as compared to carbon monoxide on platinum {111}. The lack of structural literature would make interpretation of the stress results questionable. However, upon completion of structural study, such as by LEED, interpretation would be possible and scientific value derived from the results.

8.3 Future Works for Carbon Monoxide on Platinum

On the subject of carbon monoxide on platinum {111}, one of the main driving forces for work in the system is the catalytic activity of platinum {111} and the role of so called "poisoning" species like carbon monoxide on that catalytic activity. Future work could consist of the adsorption of oxygen on platinum {111} and the co-adsorption of carbon monoxide and oxygen on platinum {111}. By comparing the adsorption stresses of carbon monoxide, oxygen, and the combination of oxygen and carbon monoxide, it should be possible to extract the characteristic stress of interaction for adsorbed carbon monoxide and oxygen on the platinum {111} surface. This would help further understanding of carbon monoxide oxidation, which would be quite valuable. A study similar to this was conducted in electrolyte using surface stress to study how bi-functional catalysis operated, showing how surface stress is a sensitive and valuable tool in studying these phenomena (Mickelson 2009). Naturally, many other works using the DSM and the adsorption of a wide range of species could be proposed, but their execution would be similar.

8.4 Future Works for Ice Thin Films

As for ice thin films, the previously unstudied (until this work) stresses of the system are open to many possible research paths. These include wetting layer work, the transition from wetted ice to bulk ice, and the influence of foreign species. Each would prove to be an expansive area in which to conduct exploratory stress measurement work.

Studying the wetting layer of ice would be far more difficult than the carbon monoxide on platinum {111} work where a single layer of adsorption was studied. The complicating factor is the need for a clean surface combined with the need for a cold substrate. In the carbon monoxide on platinum {111} case, a fresh platinum surface could be grown, then shortly thereafter the carbon monoxide introduced and stresses recorded. This is not possible in the case of ice, as the cooling time precludes this. However, it should be possible to sputter clean the existing ice off the substrate surface using an ion gun. An ion gun is very similar to a sputter gun, but the ions are directed outward towards a sample as opposed to contained at a target surface. As long as the sputtering is rapid and does not heat the surface significantly the substrate should remain clean and equilibrate quickly. As discussed earlier in the ice literature review in Chapter 8, the wetting layer adopts various structures depending on the substrate. Each of these structures should have a markedly different stress signature associated with them. How does the chain-like growth compare to a layer-by-layer growth mode? What happens to the stress profile when those chains begin to interact? It should be possible to answer these questions if a clean adsorption surface could be guaranteed.

Leading naturally from the proposed wetting layer work is the study of the structural transition from a wetting layer to bulk ice growth. The same difficulties associated with obtaining wetting layer stresses exist for this study, but assuming that a wetting layer could be grown, there are several points of interest that could result from the study. One of the most significant is what happens to the stress

profile when the ice film begins to form crystallites. Would the stress be similar to other hetero systems that develop in the Volmer-Weber growth mode or would the wetting layer significantly impact the stresses? Also, it would be interesting to see if zipping stresses (as discussed in Chapter 3 for metallic thin films) develop when the crystallites meet. It is possible that the wetting layer could act as a mitigating factor in the development of tensile zipping stresses. The early growth of an ice film has many unanswered questions.

Finally, the effect of foreign species could be studied, such as halide ions or partial pressures of other gasses. In order to conduct these experiments another introduction tool, such as another leak valve, would be needed. This is quite straightforward, making this one of the more approachable experiments. Naturally, a large range of gasses could be simultaneously introduced with the water vapor. There is literature showing that other species change the structure of the wetting layer, which should then have a measurable stress difference when compared to pure water (Doering 1982, Sadtchenko 2000, Delval 2005. This could provide insight into chemical solvation at an interface in electrolyte. Also, an already grown amorphous structure could be exposed to species with varying strengths of adsorption. The excess surface area of the pores would then amplify the adsorption stresses, and the surface stress change of adsorption measured to an accuracy not possible with the 2D surface of the DSM.

The hypothetical works discussed above are only a fraction of possible experimental paths. Each provide a large amount of curiosity driven value and could greatly expand the current knowledge of water. It is a very prevalent, but curious molecule. Water will take a great deal of study before its complexities are finally understood.

CHAPTER 9

CONCLUDING REMARKS

9.1 Conclusion

This dissertation presented a great deal of experimental work and information from literature. After outlining the document's structure in Chapter 1, the chapter also described how surfaces become an important factor when the surface-to-volume ratio becomes high, and served as a motivation for studying surfaces. Practical drive for their study then came from the many devices that operate at the length scales where these surface effects are prominent. Chapter 2 then defined the key physical phenomena so that all later chapters could be understood in a coherent manner. Chapter 3 reviewed literature of thin metallic films grown in vacuum and the relationship between the stress and structure of those films as they grew. This gave a first look at real studies of stress-structure phenomena as well as the history of the field. Chapter 4 then covered the experimental details associated with this dissertation in a broad manner. This gave an understanding of not only how the pertinent devices operated, but also the challenges, limitations, and capabilities of vacuum. Chapter 5 was the first work done by the author, and showed how stress data could be used to infer structural evolution. In this case it was for the continued growth of a copper film on an oxygen dosed copper film. The work also showed that even sub-monolayer coverage of oxygen was enough to significantly alter the growth stresses of the copper film. Chapter 6 then showed work that pushed the limits of stress measurement by recording the stresses of a single layer of adsorbed carbon

monoxide on a platinum {111} surface. Using the innovative DSM to surmount experimental difficulties, it was shown that as periodic structures developed in the carbon monoxide adlayer, the stress behavior of the system reflected these changes. The final work presented in Chapter 7 was highly exploratory, investigating the behavior of not only a system that had yet to be explored in the realm of stress but also at cryogenic temperatures. There were many experimental difficulties in accomplishing this, but the stress results proved to link up well with the literature on structure. Important behaviors of the system during both growth and heating were then modeled, and based on both the results and modeling, possible theories on the origin of the stress signals seen were proposed. Chapter 8 then discussed possible future works for each of the 3 projects discussed in Chapters 5, 6, and 7. Discussion covered not only what experiments would be valuable to conduct, but how those experiments would be conducted and the anticipated information obtained from them. The dissertation came to a close with a recap and closing remarks in this chapter, Chapter 10.

REFERENCES

Abermann R. and Koch R. (1986), Thin Solid Films 142, 65.

Abermann R. (1990), Vacuum 41, 1279.

Blackman G. S. et al. (1988), Phys. Rev. Lett. 61, 2352.

Brown D. E. et al. (1996), J. Phys. Chem. 100, 4988.

Brown D. E. and George S. M. (1996), J. Phys. Chem. 100, 15460.

Cammarata R. C. (1994), Progress in Surface Science Vol. 46, No. 1, 1-38.

Cammarata R. C. (2000), Journal of Materials Research 15, 2468.

Campbell C. T. et al. (1980), J. Chem. Phys. 73, 5862.

Cerda J. et al. (2004), Phys. Rev. Lett. 93, 116101.

Chason E. et al. (2002), Physical Review Letters 88.

Crank J. (1975), The Mathematics of Diffusion.

Delval C. and Rossi M. J. (2004), Phys. Chem. Chem. Phys. 6, 4665.

Doering D. L. and Madey T. E. (1982), Surf. Sci. 123, 305.

Doerner M. F. and Nix W. D. (1988), CRC Critical Reviews in Solid State and Materials Sciences 14, 225.

Doljack F. A. and Hoffman R. W. (1972), Thin Solid Films 12, 71.

Engstrom E. et al. (2011), submitted to J. of the Electrochemical Society.

Einstein T. L. and J. R. Schrieffer (1973), Phys. Rev. B 7, 3629.

Einstein T. L. ed. by Unertl N. (1996), Physical Structure of Solid Surfaces.

Floro J. A. et al. (2001), Journal of Applied Physics 89, 4886.

Freund L. B. and Suresh S. (2003), Thin Film Materials.

Friesen C. and Thompson C. V. (2002), Physical Review Letters 89.

Fu Y. et al. (2004), Sensors and Actuators A 112, 395.

Gibson K. D. et al. (2000), J. Chem. Phys. 112, 9852.

Haiss W. (2001), Rep. Prog. Phys. 64, 591.

Haq S. et al. (2002) Surface Science 505, 171.

Hoffman R. W. (1966), Physics of Thin Films 3, 211, 273.

Hoffman R. W. (1976), Thin Solid Films 34, 185.

Huang R. et al. (2010), IEEE Trans. Device Mater. Reliab. 10, 47.

Kennedy J. K. and Friesen C. (2007), J. Applied Physics 101, 054904.

Kennedy J. K. and Friesen C. (2011), In Preparation.

Klockholm E. and Berry B. S. (1968), J. of the Electrochemical Society 155, 823.

Koch R. (1994), Journal of Physics: Condensed Matter 6, 9519.

Koch R. (2005), Physical Review Letters 94.

Lagally M. G. (1993), Phys. Today 46,24.

Laugier M. (1981), Vacuum 31, 155.

Ledbetter H. M. and Kim S. A. (1988), Mat. Sci. and Eng. A, 101, 87-92.

Martin M. (2010), http://www.lsbu.ac.uk/water/phase.html.

Marquardt E. D. et al. (2000), 11th International Cyrocooler Conference, June 2000, Keystone, Co.

Matsumoto T. et al. (2001), Surf. Sci. 471, 225-245.

Mays C. W. et al. (1969), Surface Science 12, 134.

Michaelides A. et al. (2003), J. Am. Chem. Soc. 125, 2746.

Mickelson L. and Friesen C. (2009), J. Am. Chem. Soc. 131, 14879.

Morgenstern M. et al. (1996), Phys. Rev. Lett. 77, 703.

Nakamura M. et al. (2000), Chem. Phys. Lett. 320, 381.

Neddermeyer H. (1990), Crit. Rev. Solid State Mater. Sci. 16, 309.

Nix W. D. and Clemens B. M. (1999), J. of Materials Research 14, 3467.

Ogletree D. F. et al. (1986), Surf. Sci. 173, 351.

Ostwald W. (1887), Lehrbuch der allgemeinen Chemie 2.

Pao C. W. et al. (2006), Physical Review B 74.

Pashley D. W. and Stowell M. J. (1966), J. Vac. Sci. Technol. 3, 156.

Petrovic J.J. (2003), J. of Mat. Science 38, 1-6.

Ramaswamy V. et al. (2001), Mater. Sci. and Eng. A319, 887.

Roelofs L. D. (1996), Physical Structure of Solid Surfaces.

Sadtchenko V. et al. (2000), J. Phys. Chem. B 104, 2511.

Seel S. C. et al. (2000), J. Apl. Phys. 88, 12.

Shuttleworth R. (1950), Proceeding of the Physical Society of London Section A, 63, 365.

Simmons R. O. and Balluffi R. W. (1957), Phys. Rev. 108, 2.

Smith R. S. et al. (1996), Surface Science 367, L13.

Spisa S. L. et al. (2001), J. Geophys. Research 106, E12, 33351.

Stafford G. R. and Bertocci U. (2009), J. Phys. Chem. C 113, 13249.

Steininger H. et al. (1982), Surf. Sci. 123, 264.

Stoney G. G. (1909), Proceedings of the Royal Society (London) A82, 172.

Thornell G. et al. (1999), IEEE Trans. on Ultrasonics, Ferroelectrics, and Frequency Control 46, 4.

Tsay J. S. et al. (2001), J. Vac. Sci. Technol. A 19, 2217.

Thürmer K. and Bartelt N. C. (2008), Phys. Rev. B 77, 195425.

Tsay J. S. et al. (2001), J. Vac. Sci. Technol. A 19, 2217.

Venables J. A. et al. (1980), Surf. Sci. 95, 411.

Verdaguer A. et al. (2006), Chem. Rev. 106, 1478.

Wilcock J. D. and Campbell D. S. (1969), J of the Mech. and Phys. of Solids 47, 1113.

Wilcock J. D. et al. (1969), Thin Solid Films 3, 13.

Wilson C. J. et al. (2007), IEEE Trans. Device Mater. Reliab. 7, 356.

Zhu X. Y. et al. (1991), J. Phys. Chem. 95, 8393.

Zinke-Allmang et al. (1992), Surface Science Reports 16, 377.

Zondlo M. A. et al. (1997), J. Phys. Chem 100, 10887.

APPENDIX A

COPYRIGHT PERMISSIONS

Copyright permission for Figure 3.2

License Number: 2761620994184

License date: Oct 03, 2011

Licensed content publisher: American Institute of Physics

Licensed content publication: Journal of Applied Physics

Licensed content title: Tensile stress evolution during deposition of Volmer–Weber thin films

Licensed content author: Steven C. Seel, Carl V. Thompson, Sean J. Hearne, Jerrold A. Floro et al.

Licensed content date: Dec 31, 1969

Volume number: 88

Issue number: 12

Type of Use: Thesis/Dissertation

Requestor type: Student

Format: Print and electronic

Portion: Figure/Table

Copyright Permission for Figure 3.5

License Number: 2761630453403

License date: Oct 03, 2011

Licensed content publisher: Elsevier

Licensed content publication: Thin Solid Films

Licensed content title: In situ study of thin film growth by internal stress

measurement under ultrahigh vacuum conditions: Silver and copper under the influence of oxygen

Licensed content author: R. Abermann,R. Koch

Licensed content date: 15 August 1986

Licensed content volume number: 142

Licensed content issue number: 1

Number of pages: 12

Type of Use: reuse in a thesis/dissertation

Portion: figures/tables/illustrations

Number of figures/tables/illustrations: 1

Format: both print and electronic

Copyright permission for Figure 3.6

License number: 2761630836434

License date: Oct 03, 2011

Licensed content publisher: Elsevier

Licensed content publication: Vacuum

Licensed content title: Measurements of the intrinsic stress in thin metal films

Licensed content author: R. Abermann

Licensed content date: 1990

Licensed content volume number: 41

Licensed content issue number: 4-6

Number of pages: 4

Type of Use: reuse in a thesis/dissertation

Portion: figures/tables/illustrations

Number of figures/tables/illustrations: 1

Format: both print and electronic

Copyright permission for Figure 5.1, Figure 5.2, Figure 5.3, Figure 5.4, Figure 5.5, and Figure 5.6

License Number: 2761640143950

License date: Oct 03, 2011

Licensed content publisher: American Institute of Physics

Licensed content publication: Journal of Applied Physics

Licensed content title: The effect of oxygen adsorption on Cu{111} thin film growth stresses

Licensed content author: J. K. Kennedy, C. Friesen

Licensed content date: Mar 6, 2007

Volume number: 101

Issue number: 5

Type of Use: Thesis/Dissertation

Requestor type: Author (original article)

Format: Print and electronic

Portion: Figure/Table

Number of figures/tables: 6

Copyright permission for Figure 6.4

License number: 2761631185794

License date: Oct 03, 2011

Licensed content publisher: Elsevier

Licensed content publication: Surface Science

Licensed content title: On the adsorption of CO on Pt(111)

Licensed content author: H. Steininger,S. Lehwald,H. Ibach

Licensed content date: 2 December 1982

Licensed content volume number: 123

Licensed content issue number: 2-3

Number of pages: 19

Type of Use: reuse in a thesis/dissertation

Portion: figures/tables/illustrations

Number of figures/tables/illustrations: 1

Format: both print and electronic

Copyright permission for Figure 7.1, 7.2, 7.4, 7.5

“Readers may view, browse, and/or download material for temporary copying purposes only, provided these uses are for noncommercial personal purposes.

Except as provided by law, this material may not be further reproduced, distributed, transmitted, modified, adapted, performed, displayed, published, or sold in whole or part, without prior written permission from the American Physical Society."

AMERICAN PHYSICAL SOCIETY
One Physics Ellipse, College Park, MD 20740 - http://www.aps.org

October 11, 2011

Jordan K. Kennedy
Arizona State University

Ref # 10647

Thank you for your permission request dated October 3, 2011. We are pleased to grant you a non-exclusive, non-transferable permission, English rights, limited to **print and electronic format**, provided you meet the criteria outlined below. Permission is for a one-time use and does not include permission for future editions, updates, databases, translations, or any other matters. Permission must be sought for each additional use. This permission does not include the right to modify APS material.

Please print the required copyright credit line on the first page that the material appears: "Reprinted (abstract/excerpt/figure) with permission from [FULL REFERENCE CITATION] as follows: authors names, journal title, volume number, page number and year of publication. Copyright (YEAR) by the American Physical Society.

The following language must appear somewhere on the website: "Readers may view, browse, and/or download material for temporary copying purposes only, provided these uses are for noncommercial personal purposes. Except as provided by law, this material may not be further reproduced, distributed, transmitted, modified, adapted, performed, displayed, published, or sold in whole or part, without prior written permission from the American Physical Society."

Provide a hyperlink from the reprinted APS material (the hyperlink may be embedded in the copyright credit line). APS's link manager technology makes it convenient and easy to provide links to individual articles in APS journals. For information, see: http://link.aps.org/.

You must also obtain permission from at least one of the authors for each separate work, if you haven't done so already. The author's name and address can be found on the first page of the published Article.

Use of the APS material must not imply any endorsement by the American Physical Society.

Permission is granted for use of the following APS material only:

- Fig. 1, Phys. Rev. Lett. 77, 703 (1996)
- Fig. 1, Phys. Rev. Lett. 93, 116101 (2004)
- Figs. 2, 3, Phys. Rev. B 77, 195425 (2008)

Permission is limited to the single title specified or single edition of the publication as follows:

- Dissertation by Jordan K. Kennedy to be published by Arizona State University

If you have any questions, please refer to the Copyright FAQ at: http://publish.aps.org/copyrightFAQ.html or send an email to assocpub@aps.org.

Sincerely,

Eileen LaManca

Eileen LaManca
Publications Marketing Coordinator

Copyright permission for Figure 7.3

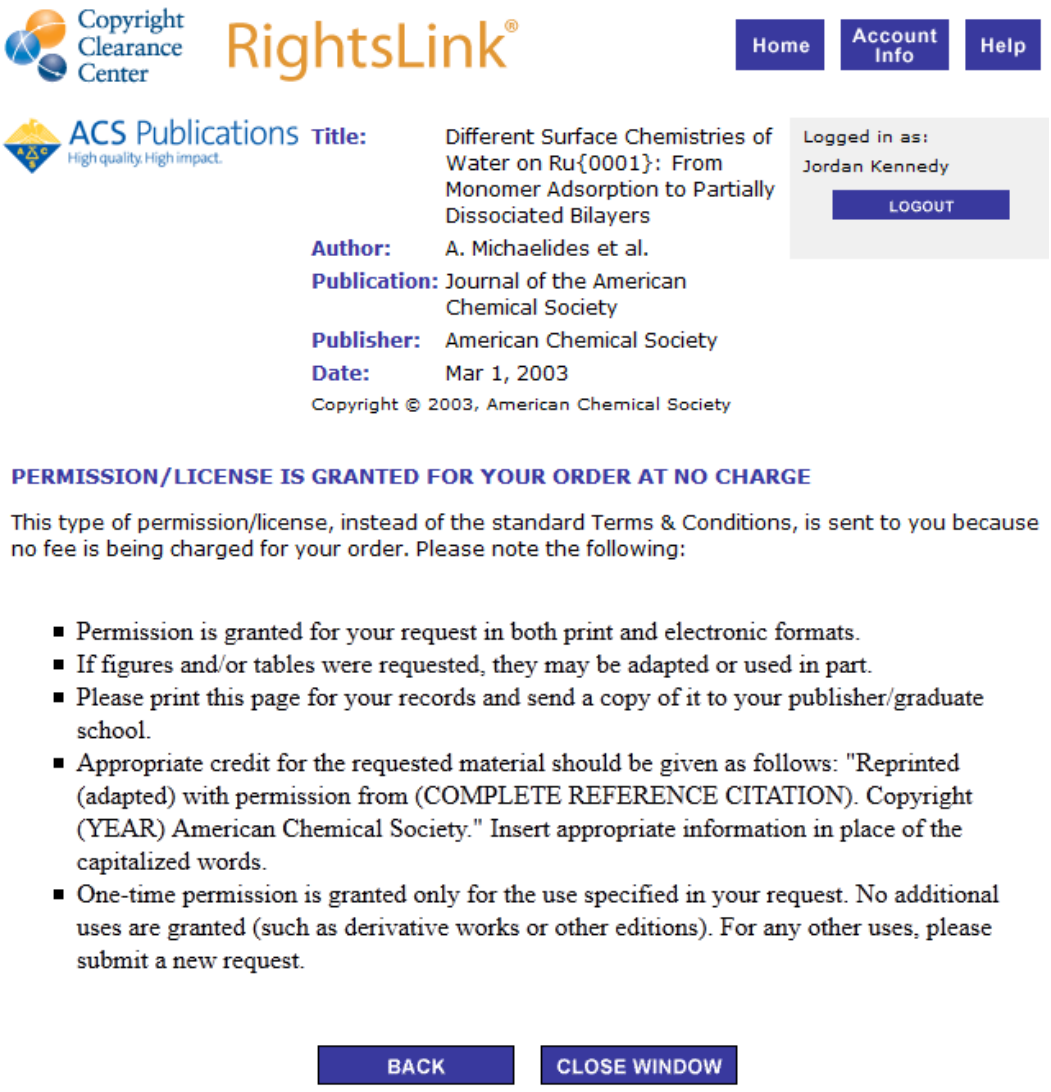

Copyright permission for Figure 7.11

License number: 2761651490591

License date: Oct 03, 2011

Licensed content publisher: Elsevier

Licensed content publication: Surface Science

Licensed content title: Desorption and crystallization kinetics in nanoscale thin films of amorphous water ice

Licensed content author: R. Scott Smith,C. Huang,E.K.L. Wong,Bruce D. Kay

Licensed content date: 10 November 1996

Licensed content volume number: 367

Licensed content issue number: 1

Type of Use: reuse in a thesis/dissertation

Portion: figures/tables/illustrations

Number of figures/tables/illustrations: 1

Format: both print and electronic